Anisotropic Response of Surface Currents to the Wind in a Coastal Region

SUNG YONG KIM

Marine Physical Laboratory, Scripps Institution of Oceanography, University of California, San Diego, La Jolla, California

BRUCE D. CORNUELLE

Climate, Atmospheric Science, and Physical Oceanography, Scripps Institution of Oceanography, University of California, San Diego, La Jolla, California

ERIC J. TERRILL

Marine Physical Laboratory, Scripps Institution of Oceanography, University of California, San Diego, La Jolla, California

(Manuscript received 10 March 2008, in final form 7 January 2009)

ABSTRACT

Analysis of coastal surface currents measured off the coast of San Diego for two years suggests an anisotropic and asymmetric response to the wind, probably as a result of bottom/coastline boundary effects, including pressure gradients. In a linear regression, the statistically estimated anisotropic response explains approximately 20% more surface current variance than an isotropic wind–ocean response model. After steady wind forcing for three days, the isotropic surface current response veers 42° ± 2° to the right of the wind regardless of wind direction, whereas the anisotropic analysis suggests that the upcoast (onshore) wind stress generates surface currents with 10° ± 4° (71° ± 3°) to the right of the wind direction. The anisotropic response thus reflects the dominance of alongshore currents in this coastal region. Both analyses yield wind-driven currents with 3%–5% of the wind speed, as expected. In addition, nonlinear isotropic and anisotropic response functions are considered, and the asymmetric current responses to the wind are examined. These results provide a comprehensive statistical model of the wind-driven currents in the coastal region, which has not been well identified in previous field studies, but is qualitatively consistent with descriptions of the current response in coastal ocean models.

1. Introduction

Surface current dynamics encompass a complex mixture of forcing terms including wind, tides, pressure gradients, and internal waves (Ewing 1950; Munk and Cartwright 1966; Essen et al. 1983; Alpers 1985; Prandle 1987; Ng 1993a,b). Generally, the wind is a dominant driving source of energy for currents, which have been considered to have an isotropic response in the open ocean (Ekman 1905; Gonella 1972; Weller 1981; Price et al. 1987; Rio and Hernandez 2003) and the coastal region (Pidgeon and Winant 2005). The coastline and bottom topography produce horizontal pressure gradients and friction so that the coastal wind response of surface currents can depend on the wind direction. Ekman (1905) introduced this anisotropy by including pressure gradients in the analysis, and Winant (2004) has made three-dimensional calculations for basins with idealized topography. However, a complete wind–ocean response model to reflect this phenomenon has not been addressed with the observation data.

The wind impulse response function (WIRF) provides a comprehensive representation of the link between the wind and currents from diurnal responses to upwelling events in the coastal region. The WIRF in the frequency domain ($\mathbf{H}$) is defined as the ratio of the Fourier coefficients of the current ($\hat{\mathbf{u}}$) to wind stress ($\hat{\boldsymbol{\tau}}$) at each frequency:

$$\mathbf{H}(z, \omega) = \frac{\hat{\mathbf{u}}(z, \omega)}{\hat{\boldsymbol{\tau}}(\omega)}. \quad (1)$$

Gonella (1972) derived the WIRF and its phase relationship at infinite and finite depth, and Weller (1981)

Corresponding author address: Sung Yong Kim, Scripps Institution of Oceanography, 9500 Gilman Dr., La Jolla, CA 92093-0213.
E-mail: syongkim@mpl.ucsd.edu

DOI: 10.1175/2009JPO4013.1

observed the current shear and matched it with the Ekman theory. Rio and Hernandez (2003) investigated the surface currents estimated by drifting buoys and the altimetry data along with atmospheric model [European Centre for Medium-Range Weather Forecasts (ECMWF)] wind stress over the global ocean. These studies (Gonella 1972; Weller 1981; Rio and Hernandez 2003) found a consistent phase relationship between surface currents and the wind. Pidgeon and Winant (2005) found negative phases between the diurnal currents and the diurnal wind at several moorings in the Santa Barbara Channel that were quantitatively consistent with previous studies. Hyder et al. (2002) used a depth-integrated slab model to examine the WIRF of the diurnal currents near the critical latitude, where the response is resonant with the diurnal wind forcing.

The time domain WIRF ($\mathbf{g}$) between the wind stress ($\boldsymbol{\tau}$) and the current ($\mathbf{u}$) at a point is defined as a convolution (Bendat and Piersol 2000):

$$\mathbf{u}(z,t) = \int_{t'} \mathbf{g}(z, t - t')\boldsymbol{\tau}(t')\,\mathrm{d}t'. \tag{2}$$

Ekman (1905), Gonella (1971), Kundu (1984), and Blackford (1978) derived the time-dependent current response for a step function wind using linear and slab models. Lewis and Belcher (2004) examined the time-dependent Ekman solutions coupled with Stokes drift using Laplace transforms to include evanescent solutions. Prandle (1987), Essen (1993), Ng (1993a), Zelenke (2005), and Rabinovich et al. (2007) parameterized the observations of the wind stress and currents using linear/nonlinear models and performed a time domain regression. Although Ng (1993a) and Rabinovich et al. (2007) introduced the possibility of an anisotropic current response, the statistical models lacked physical interpretation, and the difference in skill between isotropy and anisotropy was not explored.

Li and Weisberg (1999), Weisberg et al. (2001), and Overland and Pease (1988) discussed the anisotropic and asymmetric current (or sea ice current) response due to the sea surface height set up by the wind in the coastal regions using numerical models. Simpson et al. (2002) explained the in-phase strong current variability with an analytical two-layer model using the pressure gradient set up by the diurnal wind. Sverdrup (1938), Allen (1980), Beardsley et al. (1987), Huyer and Kosro (1987), and Choi and Wilkin (2007) also have examined the upwelling in the coastal region and the dependency of the response on the wind direction.

The three-dimensional Ekman theory—including pressure gradients induced by boundaries—can produce anisotropy, but it is difficult to apply to the realistic cases with open boundaries, complicated bathymetry, and sparse wind observations. A statistical model that substantiates the anisotropy and asymmetry of the surface current response is presented in this paper, without having to build a numerical model.

This paper is organized into three sections. First, the Ekman solutions with depth-independent viscosity are obtained for the isotropic and anisotropic WIRFs in the frequency domain (section 2). Next, the isotropic and anisotropic WIRFs are statistically estimated in both frequency and time domains using observations of surface currents and the wind (sections 3, 4, and 5b). Finally, nonlinear WIRFs are considered for their asymmetrical responses (section 5c).

2. Theoretical background

a. Momentum equations

Adjustment terms (A_x and A_y) in the momentum equations are introduced that are only related to the wind-driven currents modeling both bottom drag and pressure gradient set up along the coast:

$$\frac{\partial u}{\partial t} - f_c v + A_x = \frac{1}{\rho}\frac{\partial}{\partial z}\left(\mu\frac{\partial u}{\partial z}\right) \quad \text{and} \tag{3}$$

$$\frac{\partial v}{\partial t} + f_c u + A_y = \frac{1}{\rho}\frac{\partial}{\partial z}\left(\mu\frac{\partial v}{\partial z}\right), \tag{4}$$

where f_c, ρ, and μ denote the Coriolis frequency, the seawater density, and the dynamic viscosity, respectively. The depth coordinate (upward positive) is denoted as z. Assuming μ is independent of depth, the adjustment terms are composed of pressure gradients and the anisotropic part of the stress divergence,

$$A_x = \frac{1}{\rho}\frac{\partial p}{\partial x} - \nu_a\frac{\partial^2 u}{\partial z^2}, \tag{5}$$

$$A_y = \frac{1}{\rho}\frac{\partial p}{\partial y} - \nu_a\frac{\partial^2 v}{\partial z^2}, \tag{6}$$

where ν and ν_a denote the isotropic and anisotropic kinematic viscosity, respectively.

For the statistical analysis on the observations, the adjustment terms are considered as convolutions of the time history of currents:

$$\begin{aligned} A_x &= a_{xx} * u + a_{xy} * v \\ &= \int_{-\infty}^{\infty} a_{xx}(\xi)u(t-\xi) + a_{xy}(\xi)v(t-\xi)\mathrm{d}\xi, \end{aligned} \tag{7}$$

$$\begin{aligned} A_y &= a_{yx} * u + a_{yy} * v \\ &= \int_{-\infty}^{\infty} a_{yx}(\xi)u(t-\xi) + a_{yy}(\xi)v(t-\xi)\mathrm{d}\xi, \end{aligned} \tag{8}$$

where a_{xx}, a_{xy}, a_{yx}, and a_{yy} represent the effects of the bottom and coastline boundary friction and the pressure gradient set up near the coast. They are convolved in the time domain with the current components (u and v) in the x and y directions, respectively (The asterisk is the time domain convolution operator.).

Since the system is linear and time invariant, it is natural to work in the frequency domain, and the equations transformed into the frequency domain are simpler because convolutions become products:

$$(i\omega + a_{xx})\hat{u} + (-f_c + a_{xy})\hat{v} = \nu\frac{\partial^2\hat{u}}{\partial z^2}, \tag{9}$$

$$(f_c + a_{yx})\hat{u} + (i\omega + a_{yy})\hat{v} = \nu\frac{\partial^2\hat{v}}{\partial z^2}. \tag{10}$$

The isotropic and anisotropic WIRFs in the frequency domain are calculated explicitly (section 2b and appendix A1) and numerically (section 2c and appendix A2), respectively. The isotropic WIRF is represented by a single complex function in both frequency and time domains, and the anisotropic WIRF consists of four complex functions in the frequency domain or four real functions in the time domain.

b. Isotropic approach

If an isotropic response is expected, the momentum equations can be combined using complex numbers to represent the surface currents ($\mathbf{u} = u + iv$) and wind stress ($\boldsymbol{\tau} = \tau_x + i\tau_y$). The frequency domain isotropic WIRF (FIWIRF) at finite depth with the depth-independent viscosity and adjustment terms is reviewed in appendix A1.

As a simpler form, the FIWIRF for water of infinite depth without adjustment terms ($A_x = A_y = 0$) was derived as in Ekman (1905) or textbooks:

$$\mathbf{H}(z,\omega) = \frac{\hat{\mathbf{u}}(z,\omega)}{\hat{\boldsymbol{\tau}}(\omega)} = \frac{e^{\lambda z}}{\lambda\rho\nu}, \tag{11}$$

where $\lambda = \sqrt{i(\omega + f_c)/\nu}$. The depth at which the current is directed opposite to the surface current at zero frequency is $\delta_E = \pi\sqrt{2\nu/f_c}$ (Ekman 1905), which we call the Ekman depth. Typical eddy viscosity (ν) values for the upper ocean used in these calculations have ranged from 10^{-5} to 10^{-1} m^2 s^{-1} (Santiago-Mandujano and Firing 1990; Chereskin 1995; Weller and Plueddemann 1996; Schudlich and Price 1998; Rio and Hernandez 2003). The analysis below is not sensitive to the choice of eddy viscosity, so 1×10^{-4} m^2 s^{-1} is chosen as an example.

The magnitude and phase of the FIWIRF at quarter fractions of the Ekman depth ranging from the surface to the Ekman depth are shown in Figs. 1a and 1c, respectively. The current response is infinite at $\omega = -f_c$ [f_c = 1.07 cycles per day (cpd) in the study domain] and weakens with depth as a result of the decreasing momentum flux divergence (Fig. 1a). The veering of surface currents is to the left of the wind stress with positive phase ($\omega < -f_c$) and to the right of the wind stress with negative phase ($\omega > -f_c$) (Gonella 1972; Weller 1981; Rio and Hernandez 2003). The phase of the FIWIRF at the surface is a step function with a jump from 45° to −45° at $\omega = -f_c$ (Fig. 1c). The veering of the current profile under steady wind ($\omega = 0$) is 45° to the right of the wind at the surface and opposite to the surface current (225°) at the Ekman depth (Ekman 1905; Gonella 1971). The current rotates clockwise ($\omega < -f_c$) with depth and counterclockwise ($\omega > -f_c$), respectively.

The WIRF is dependent on the viscosity as expressed by δ_E in the simple cases. The WIRF with lower viscosity has a stronger response at the surface and decays faster with depth yielding shallow momentum penetration into the water column. For example, a well-stratified water column with a shallow pycnocline is likely to have a strong wind impulse response confined near the surface, as with diurnal jets (Price et al. 1986) or in the summer. In the same way, the current response due to the wind in a water column with higher viscosity is weaker at the surface and penetrates more deeply, as with well-mixed layers in the winter.

The difference between WIRFs for the surface current assuming infinite or finite depth is small. The adjustment terms generally reduce the magnitude of the WIRF due to damping, removing the singularity at the Coriolis frequency.

c. Anisotropic approach

The bottom friction and pressure set up in the momentum equations can be different in the x and y directions and can lead to an anisotropic current response, referred to as ''extended Ekman theory'' in the following. The surface currents and the wind are considered as two-dimensional vectors as in Pedlosky (1992) instead of as scalar complex variables. Although the adjustment terms can be functions of frequency, for many of the following examples they are assumed to be constant in the frequency domain corresponding to Rayleigh friction in the time domain $a_{xx} = r_{xx}\delta(t)$, $a_{yy} = r_{yy}\delta(t)$, and $a_{xy} = a_{yx} = 0$ [$\delta(t)$ denotes the dirac delta function]. The frequency domain anisotropic WIRF (FAWIRF) at finite depth is calculated algebraically in appendix A2.

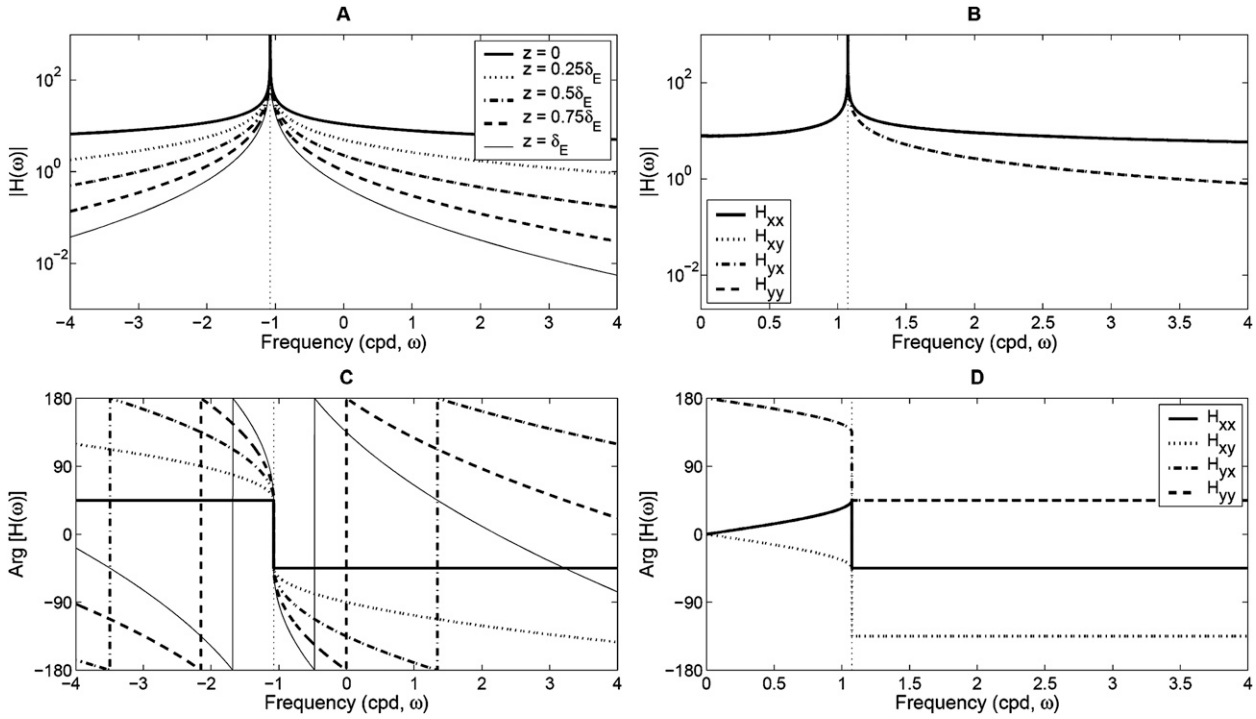

FIG. 1. (a),(c) The magnitude and phase of the linear FIWIRF in the Ekman theory at each 0.25 δ_E depth increment from the surface ($z = 0$) to the Ekman depth ($z = \delta_E$). (b),(d) The magnitude and phase of the four functions of the linear FAWIRF at the surface for a parameter choice as the Ekman theory. The FIWIRF and FAWIRF are calculated assuming infinite water depth with depth-independent viscosity ($\nu = 1 \times 10^{-4}\ \mathrm{m^2\ s^{-1}}$) and no friction ($r_{xx} = 0$ and $r_{yy} = 0$). The terms H_{xx} and H_{yy} in (b) and (d) are superposed, and H_{xy} and H_{yx} in (b) are superposed. The vertical dotted line indicates the inertial frequency ($\omega = \pm 1.07$ cpd) in the study domain.

As an introduction to the form of the anisotropic solutions, the FAWIRF at infinite depth with no adjustment terms was calculated, and its magnitude and phase are shown in Figs. 1b and 1d, respectively. The current responses resulting from two wind impulses and four components of the FAWIRF are presented as

$$\hat{u}(z,\omega) = H_{xx}(z,\omega)\hat{\tau}_x(\omega) + H_{xy}(z,\omega)\hat{\tau}_y(\omega), \tag{12}$$

$$\hat{v}(z,\omega) = H_{yx}(z,\omega)\hat{\tau}_x(\omega) + H_{yy}(z,\omega)\hat{\tau}_y(\omega), \tag{13}$$

where H_{xx}, H_{xy}, H_{yx}, and H_{yy} are complex functions in the frequency domain. This solution is the same as the Ekman solution. Although the anisotropic responses are not as convenient to interpret, they can be converted to rotary spectra for comparisons with the isotropic response. In this FAWIRF, the magnitudes of all four terms are the same for $\omega < f_c$, and the magnitudes of the diagonal terms (H_{xx} and H_{yy}) and the cross terms (H_{xy} and H_{yx}) are the same for $\omega > f_c$, respectively (Fig. 1b). The cross terms are out of phase, while the diagonal terms are in phase for all frequencies. The phase slopes ($\partial\theta/\partial\omega$) of the cross terms and diagonal terms have an opposite sign for $\omega < f_c$ and zero for $\omega > f_c$ (flat phase).

The anisotropic WIRF can be represented in the same way as the isotropic WIRF by computing the response to each directional wind component separately. For example, the surface current responses ($\hat{u}$ and $\hat{v}$) can be expressed as the combination of the four functions of the FAWIRF multiplied by the wind stress components ($\hat{\tau}_x$ or $\hat{\tau}_y$) in the negative frequency (clockwise, $\omega < 0$) and the positive frequency (counterclockwise, $\omega > 0$) domains:

$$\hat{\mathbf{u}}(\omega < 0) = (H^{\dagger}_{xx} + iH^{\dagger}_{yx})\hat{\tau}_x(\omega), \tag{14}$$

$$\hat{\mathbf{u}}(\omega > 0) = (H_{xx} + iH_{yx})\hat{\tau}_x(\omega), \tag{15}$$

$$\hat{\mathbf{u}}(\omega < 0) = (H^{\dagger}_{xy} + iH^{\dagger}_{yy})\hat{\tau}_y(\omega), \quad \text{and} \tag{16}$$

$$\hat{\mathbf{u}}(\omega > 0) = (H_{xy} + iH_{yy})\hat{\tau}_y(\omega), \tag{17}$$

where † denotes the complex conjugate and $\hat{\mathbf{u}}$ is the rotary Fourier coefficients for u and v. This enables the plotting of the FAWIRF in Figs. 2b and 2d as the FIWIRF for the Ekman theory (Figs. 1a and 1c). As an example, the surface current response at $\omega = 0$ is 45° to the right of the wind stress:

$$\hat{u} + i\hat{v} = H_{xx}(0)\hat{\tau}_x + H_{xy}(0)\hat{\tau}_y + i[H_{yx}(0)\hat{\tau}_x + H_{yy}(0)\hat{\tau}_y] \tag{18}$$

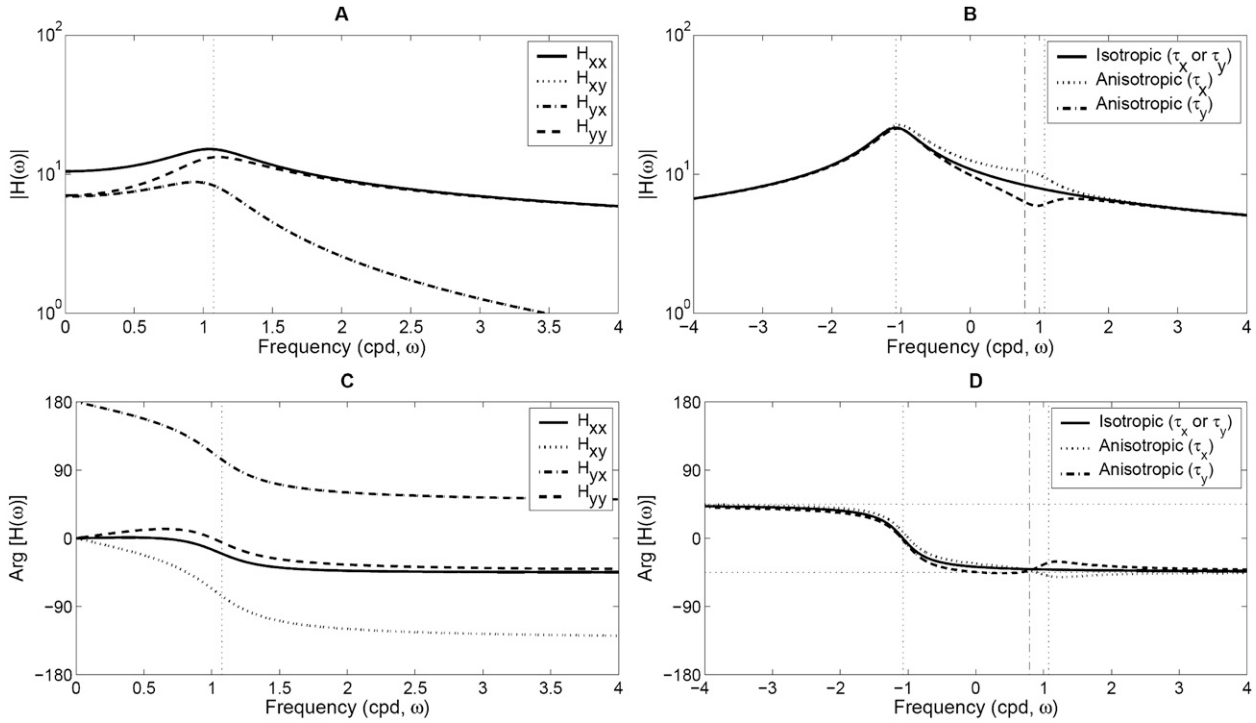

FIG. 2. The linear FAWIRF based on the extended Ekman theory with depth-independent viscosity ($\nu = 1 \times 10^{-4}$ m^2 s^{-1}) and two different frictions in the x and y directions ($r_{xx} = 1 \times 10^{-6}$ s^{-1} and $r_{yy} = 4 \times 10^{-5}$ s^{-1}). (a) The magnitude of the FAWIRF. (b) The magnitude of the FIWIRF with same viscosity and the friction as the arithmetic mean of two frictions [$r = (r_{xx} + r_{yy})/2$], and the magnitude of the FAWIRF when wind stress (τ_x and τ_y) is applied in each direction. (c) The phase of the FAWIRF. (d) The phase of the FIWIRF and FAWIRF. The phase transition frequency (ω_0) is 0.7909 cpd [a vertical dashed–dotted line in (b) and (d)] for the selected parameters. The terms H_{xy} and H_{yx} in (a) are overlapped. See Fig. 1 for definition of the vertical dotted line.

$$= |H_{xx}(0)|e^{-\pi/4}(\hat{\tau}_x + i\hat{\tau}_y), \tag{19}$$

where $H_{xx}(0) = H_{yy}(0) = H_{xy}(0) = -H_{yx}(0)$ as shown in Figs. 1b and 1d. The FIWIRF and FAWIRF in Fig. 1 are used for comparison to the WIRFs estimated from the observation data (Figs. 6, 7, 12, and 13).

When the adjustment terms are different in the x and y directions ($r_{xx} < r_{yy}$ in this example), the response to either x- or y-directional wind stress using the FAWIRF is compared with that of the FIWIRF with friction equal to the arithmetic mean of the two frictions [$r = (r_{xx} + r_{yy})/2$]. The symmetry in the FAWIRF is broken by the differing friction (Figs. 2a and 2c), although the magnitudes of the cross terms (a_{xy} and a_{yx}) of the adjustment terms are included as the identical amount. The peaks of the FAWIRF are spread, and the phases become smooth. Using Eqs. (14)–(17), the FAWIRF for each wind stress component is converted to compare with the FIWIRF (Figs. 2b and 2d). The magnitude and phase of the isotropic WIRF stay between the two components of the anisotropic WIRF. Because of the damping by the friction, the magnitude of the FAWIRF in the direction with more friction is smaller than that in the direction with less friction (Fig. 2c).

The phase transition of the FAWIRF can be examined in three frequency bands, as shown in Fig. 2d: The current response in the direction with less friction is more to the left of the wind than that in the direction with more friction for $\omega < -f_c$. The current response in the direction with more friction is more to the right of the wind than that in the direction with less friction for $\omega > -f_c$ but less than the frequency ω_0 where the phase curves cross ($-f_c < \omega < \omega_0$). In other words, more friction leads to more veering angle in the low-frequency band ($|\omega| < f_c$), as expected. The phase transition frequency (ω_0) varies between $f_c/2$ and f_c as a function of the two frictions (not shown). Above the transition frequency, the current in the direction with less friction is more to the right of the wind than the current response in the direction with more friction. Both anisotropic surface current responses converge to $-45°$ as $\omega \to \infty$.

When the adjustment terms are isotropic ($r_{xx} = r_{yy}$), the solution is isotropic, so the FIWIRF and FAWIRF are identical. The magnitude of the four terms of the FAWIRF show similar patterns to the Ekman theory, except for a blunt peak at the Coriolis frequency and the

smoothly changing phase as a result of the nonzero friction. The phase slope at $\omega = -f_c$ of the FIWIRF and FAWIRF (all four functions) is reduced in magnitude as the friction coefficient (r) increases:

$$\left.\frac{\partial\theta(\omega, r=0)}{\partial\omega}\right|_{\omega=-f_c} = -\infty, \tag{20}$$

$$\left.\frac{\partial\theta(\omega, r\to\infty)}{\partial\omega}\right|_{\omega=-f_c} \to 0. \tag{21}$$

As the friction increases, the phase at $\omega = 0$ becomes bigger than $-45°$, which means the surface wind-driven currents are heading less than 45° to the right of the wind.

3. Methods

a. Statistical linear estimate of WIRFs

The isotropic and anisotropic WIRFs in both frequency and time domains are estimated using the observations of surface currents and wind stress. Four cases are considered: FIWIRF and FAWIRF and time domain isotropic and anisotropic WIRFs (TIWIRF and TAWIRF). Although in ideal cases the frequency and time domain estimates should be equivalent, the treatment of missing data leads to differences, and so both methods are used as a check on the results and as a measure of uncertainty. This statistical estimate employs a form of ridge regression (Hoerl and Kennard 1970; Marquardt 1970; Snee 1977; Golub et al. 1979) using regularization. The wind stress and surface currents in bold font in the following equations means either a complex number in the isotropic case or a two-element vector in the anisotropic case.

1) FREQUENCY DOMAIN

From Eq. (1), the linear regression equation in the frequency domain is

$$\hat{\mathbf{u}}(z,\omega) = \mathbf{H}(z,\omega)\hat{\boldsymbol{\tau}}(\omega). \tag{22}$$

The frequency domain WIRF ($\mathbf{H}$) is computed from the (time) ensemble covariance average of the Fourier coefficients of surface currents ($\hat{\mathbf{u}}$) and wind stress ($\hat{\boldsymbol{\tau}}$) at each frequency (ω):

$$\mathbf{H}(z,\omega) = [\langle\hat{\mathbf{u}}(z,\omega)\hat{\boldsymbol{\tau}}^{\dagger}(\omega)\rangle][\langle\hat{\boldsymbol{\tau}}(\omega)\hat{\boldsymbol{\tau}}^{\dagger}(\omega)\rangle + \mathbf{R_a}]^{-1}, \tag{23}$$

where † indicates the complex conjugate transpose, $\langle\cdot\rangle$ is the ensemble average, and $\mathbf{R_a}$ is the regularization matrix and is assumed to be the noise level of the wind stress.

2) TIME DOMAIN

From Eq. (2), the covariance of currents and wind stress is

$$\langle\mathbf{u}\boldsymbol{\tau}^{\dagger}\rangle = \int_{t'}\mathbf{g}(z,t-t')\langle\boldsymbol{\tau}(t')\boldsymbol{\tau}(t)^{\dagger}\rangle\mathrm{d}t' \tag{24}$$

and is truncated and discretized as a finite sum:

$$\langle\mathbf{u}\boldsymbol{\tau}^{\dagger}\rangle = \sum_{k=0}^{N}\mathbf{g}(z,k\Delta t)\langle\boldsymbol{\tau}(t-k\Delta t)\boldsymbol{\tau}(t)^{\dagger}\rangle. \tag{25}$$

In other words,

$$\langle\mathbf{u}(z,t)\boldsymbol{\tau}_N^{\dagger}(t)\rangle = \mathbf{G}(z)\langle\boldsymbol{\tau}_N(t)\boldsymbol{\tau}_N^{\dagger}(t)\rangle, \tag{26}$$

where $\boldsymbol{\tau}_N(t) = [\boldsymbol{\tau}(t-N\Delta t)\cdots\boldsymbol{\tau}(t-\Delta t)\ \boldsymbol{\tau}(t)]^{\dagger}$ is the wind stress stacked with N hours time lag.

The time domain WIRF ($\mathbf{G}$) is computed from the covariance matrix between surface currents ($\mathbf{u}$) and time lag wind stress ($\boldsymbol{\tau}_N$):

$$\mathbf{G}(z) = [\langle\mathbf{u}(z,t)\boldsymbol{\tau}_N^{\dagger}(t)\rangle][\langle\boldsymbol{\tau}_N(t)\boldsymbol{\tau}_N^{\dagger}(t)\rangle + \mathbf{R_b}]^{-1}, \tag{27}$$

where $\mathbf{G} = [\mathbf{g}_1\,\mathbf{g}_2\cdots\mathbf{g}_N]^{\dagger}$, and $\mathbf{R_b}$ is the regularization matrix, which compensates for the sample error in the covariance matrix by suppressing small or negative eigenvalues.

b. Statistical nonlinear estimate of WIRFs

Because the responses of the linear WIRFs to oppositely directed wind are symmetric, nonlinear WIRFs are needed to break the symmetry of the response. The nonlinear WIRFs are calculated in the frequency and time domains similarly to the linear WIRFs. The magnitude of the wind stress is used in the regression to provide the nonlinear term as one of a number of ways to do the nonlinear regression. In the frequency domain the nonlinear regression equation is

$$\hat{\mathbf{u}}(z,\omega) = \mathbf{H_1}\hat{\boldsymbol{\tau}} + \mathbf{H_2}|\hat{\boldsymbol{\tau}}|, \tag{28}$$

where $\mathbf{H_1} = \mathbf{H_1}(z,\omega)$ and $\mathbf{H_2} = \mathbf{H_2}(z,\omega)$. In the time domain, the regression equation becomes

$$\mathbf{u}(z,t) = \mathbf{G_1}\boldsymbol{\tau}_N + \mathbf{G_2}|\boldsymbol{\tau}_N|, \tag{29}$$

where $\mathbf{G_1} = \mathbf{G_1}(z)$ and $\mathbf{G_2} = \mathbf{G_2}(z)$. These are performed in practice by appending the vector of $|\hat{\boldsymbol{\tau}}|$ or $|\boldsymbol{\tau}_N|$ to the existing vector data and regressing as usual.

c. Residual variance ratio estimate

The variance ratio of the wind-driven currents to the total currents at each frequency is the coherence (γ^2). The residual variance ratio (β^2) is its complement ($\beta^2 = 1 - \gamma^2$) (Bendat and Piersol 2000). The total residual variance ratio (ϵ^2) is defined as the variance of the residual currents after the wind regression to the total

currents for all frequencies or time lags and is convenient to compare the performance of the WIRFs.

1) FREQUENCY DOMAIN

The residual variance ratio in the frequency domain is

$$\beta^2(\omega) = \frac{|\hat{\mathbf{r}}(\omega)|^2}{|\hat{\mathbf{u}}(\omega)|^2}, \tag{30}$$

where $\hat{\mathbf{r}}(\omega) = \hat{\mathbf{u}}(\omega) - \mathbf{H}(\omega)\hat{\boldsymbol{\tau}}(\omega)$, and $\mathbf{H}(\omega)$ can be the FIWIRF or FAWIRF. For the linear FAWIRF, the residual variance ratios (β_u^2 and β_v^2) for the current components (u and v) are

$$\beta_u^2(\omega) = \frac{\left|H_{xx}\hat{\tau}_x + H_{xy}\hat{\tau}_y - \hat{u}\right|^2}{|\hat{u}|^2}, \tag{31}$$

$$\beta_v^2(\omega) = \frac{\left|H_{yx}\hat{\tau}_x + H_{yy}\hat{\tau}_y - \hat{v}\right|^2}{|\hat{v}|^2}, \tag{32}$$

respectively, where H_{xx}, H_{xy}, H_{yx}, and H_{yy} are the four response functions of the FAWIRF. The residual variance ratio of total currents is estimated as

$$\beta^2(\omega) = \frac{\left|H_{xx}\hat{\tau}_x + H_{xy}\hat{\tau}_y - \hat{u}\right|^2 + \left|H_{yx}\hat{\tau}_x + H_{yy}\hat{\tau}_y - \hat{v}\right|^2}{|\hat{u}|^2 + |\hat{v}|^2}. \tag{33}$$

The total residual variance ratio in the frequency domain is

$$\epsilon^2 = \frac{\sum_k |\hat{\mathbf{r}}(\omega_k)|^2}{\sum_k |\hat{\mathbf{u}}(\omega_k)|^2}. \tag{34}$$

2) TIME DOMAIN

The total residual variance ratio in the time domain is

$$\epsilon^2 = \frac{\sum_k \langle \mathbf{r}(t_k) \rangle^2}{\sum_k \langle \mathbf{u}(t_k) \rangle^2}, \tag{35}$$

where $\mathbf{r}(t) = \mathbf{u}(t) - \mathbf{G}(z)\boldsymbol{\tau}_N(t)$, $\mathbf{G}(z)$ denotes the TIWIRF or TAWIRF, and $\boldsymbol{\tau}_N(t)$ is the N hours time-lag stacked wind stress. In the ideal case, the total residual variance ratio in both frequency and time domains should be identical.

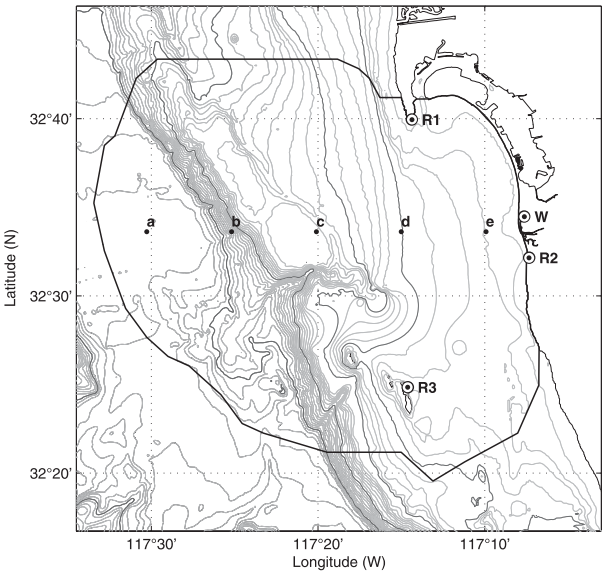

FIG. 3. The study domain of surface currents and the wind. The effective spatial coverage area where the HF radars (R1, R2, and R3) observed is indicated with black curve. Three HF radar sites are Point Loma (R1), Border Park (R2), and Coronado Island (R3). The Tijuana River wind station (W) is located near the Tijuana River valley. Five evenly spaced grid points are chosen as the (a) offshore and (e) onshore locations in the cross-shelf direction to examine the spatial variation of WIRFs (see section 5b). The bottom bathymetry contours are indicated by the thin curves with 10 m ($0\text{ m} < z < 100\text{ m}$) and 50-m ($100\text{ m} < z < 1000\text{ m}$) contour intervals and by the thick curves at the 50-, 100-, 500-, and 1000-m depths.

4. Observations

Surface currents used for this study were observed by high-frequency (HF; ~25 MHz) radars for two years (April 2003–March 2005) over a 40-km region from the coast of southern San Diego County (Kim et al. 2007, 2008). A time series of spatially averaged hourly surface currents (u and v) over the area shown as the black curve in Fig. 3 is used in this analysis. This area indicates grid points with data present for at least 70% of the two years. The spatially averaged surface current is smoother and more reliable, having only 2.2% missing data. Regional averages or point measurements can be used to investigate the horizontal structure of the WIRF. The effective averaging depth for surface current measurements by HF radar has been estimated as 5%–16% of the wavelength of the backscattering surface waves (Stewart and Joy 1974; Barrick et al. 1977; Ha 1979; Fernandez et al. 1996), but the range accepted in the HF radar community is 8%–16% (Don Barrick 2008, personal communication). Therefore, the averaging depth in this study is assumed to be approximately 1 m. The 2-yr surface current time series is detided at the main tidal constituents (O_1 P_1 K_1 M_2 and S_2) using least squares fitting. The S_2

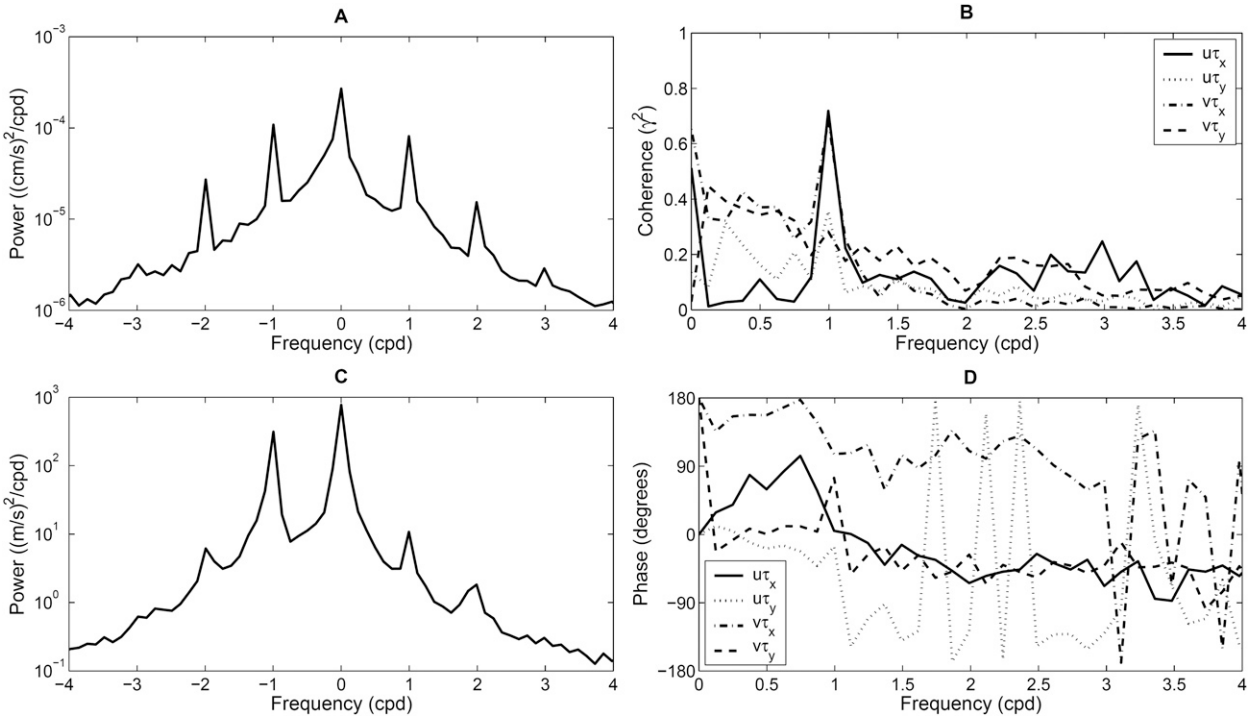

FIG. 4. The rotary power spectra of the (a) detided surface current and (c) wind are estimated from 90 subsamples with the same record length (8.12 days) and averaged across each frequency. (b) Coherence and (d) phase between the surface current and wind stress are estimated using the same spectra.

component of the surface current is removed even though the harmonic forcing of the diurnal wind can be ambiguous with the S_2 tide. The amplitude of the S_1 surface tide in San Diego is nearly zero [harmonic constituents of surface tides from NOAA (2006) and S. Y. Kim (2009)], so most of the diurnal variability of surface currents is assumed to result from the diurnal wind.

The wind observed at Tijuana River (Tidal Linkage station, Fig. 3) during the same period as the surface current is hourly averaged and has 8.5% missing data. The hourly composite mean of the wind (regardless of local sunrise and sunset; not shown) shows about 2.5 times stronger variance of the east–west wind than the north–south wind. The wind stress is estimated from the drag coefficient as described in Large and Pond (1981), and the overall results are not sensitive to the choice of the drag coefficient, except for a compensating shift in magnitude of the WIRF.

The rotary power spectra of the detided surface current and the wind are shown in Figs. 4a and 4c, respectively, which are estimated from 90 subsamples with the same record length, and missing observation values have been filled with zeros. Both have a red spectrum, and the wind spectrum shows dominant clockwise diurnal variance. Although the variance of the surface current has been reduced by the tidal fit, the resolution ($\Delta\omega = 0.1244$ cpd) of the subsample power spectrum is not enough to isolate the tidal lines, so there are broad variance peaks around the K_1 and M_2 frequencies due to nonlinearity.

The coherence and phase between each component of the surface current and wind stress are shown in Figs. 4b and 4d, which are estimated in the same way as the power spectra in Figs. 4a and 4c. The x-directional wind stress (τ_x) is coherent with surface current components (u and v) as ~0.7 near 1 cpd, and the coherence of the y-directional wind stress (τ_y) is ~0.3 at the same frequency but high at low frequencies (less than 1 cpd; Fig. 4b). The phases fluctuate at the frequencies with low coherence (Fig. 4d).

The coastline south of San Diego is aligned roughly north–south and faces west (Fig. 3). The Coronado embayment (San Diego Bay) and the headland (Point Loma) are located near the northeast boundary. The water depth of the continental shelf region is mostly less than 100 m.

5. Data analysis

a. Overview

The WIRF estimates are affected by the treatment of the missing data. The frequency domain WIRFs are estimated through replacing missing data with zeros. This

leads to positive-definite matrices, but the variances are biased low and the spurious high-frequency energies are created. The time domain WIRFs are estimated from the covariance matrix of the observed data only. This reduces bias but can create small or negative eigenvalues of the lagged covariance matrix. A regularization matrix can be added [Eqs. (23) and (27)] to limit the structure of the solutions and to make the sample autocovariance matrix of the wind stress invertible when it is nonpositive definite. This regularization keeps the regression from overfitting the data and is checked by cross validation (Efron and Gong 1983; LeBlanc and Tibshirani 1996). In other words, the model estimated from training data is applied to independent test data, and the difference between the estimated and observed data is called the cross-validation error. This error is a function of the regularization and has a minimum value between underfitting and overfitting. The regularization matrix [$\mathbf{R_a} = \mathbf{R_a}(\omega)$] in the frequency domain can be justified as the statistical and observational noise contributions to the wind stress variance. The regularization matrix in the time domain compensates for the statistical and observational noise in the autocovariance matrix of the wind. For lack of better assumptions, it is assumed to be a scaled diagonal matrix with a fraction of the wind stress variance ($\mathbf{R_a} = \kappa^2\mathbf{I}$) . The effects of missing observations on the WIRF estimate are discussed in section 6.

The goal of the regularization is to ensure that the cross-validation error is no larger than the error on the training data by adjusting $\mathbf{R_a}$ to minimize the cross-validation error for every set of predicting variables (Marquardt 1970; Hoerl and Kennard 1970). The number of subsamples in the frequency or time domain calculation increases as the length of data chunks decreases, and the degrees of freedom decrease with increasing fast Fourier transform (FFT) length or decreasing maximum time lag. The larger the maximum time lag, the more variables available to fit the data, so the total residual variance ratio decreases, but the decrease is small after about six days (Fig. 5b). Without cross validation, the error using a small number of subsamples (many fitting variables) is artificially low (Davis 1985) if regularization is not used, but the need for regularization decreases as the number of subsamples increases. As the fit is generalized from isotropic to anisotropic and then to nonlinear, the number of parameters available to fit the data increases, so the residual variance ratio without cross validation decreases. The regularization is adjusted so that the training and test datasets yield nearly the same error variance ratio. However, the residual variance ratio for the cross-validation data has larger uncertainty as a result of the limited number of realizations compared to the training data when errors are

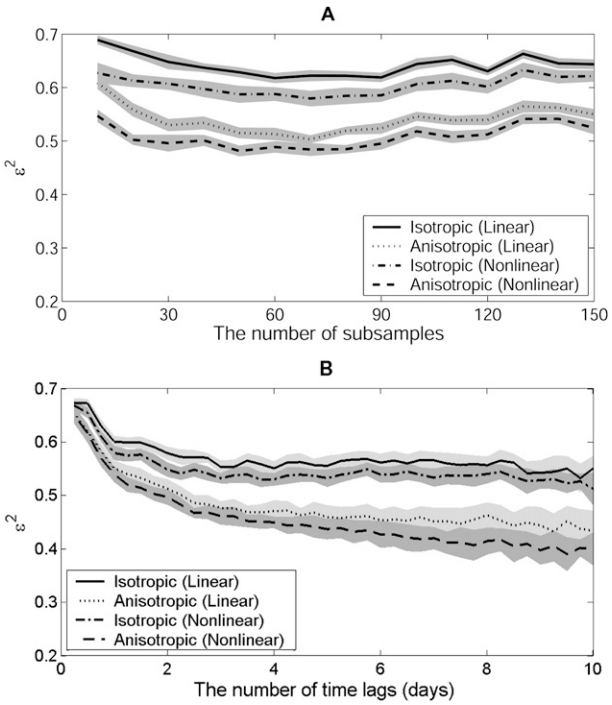

FIG. 5. (a) The total residual variance ratio (ϵ^2) of the linearly/nonlinearly estimated FIWIRFs and FAWIRFs for the training datasets in terms of the number of subsamples [Eq. (34)]. (b) The total residual variance ratio of the linearly/nonlinearly estimated TIWIRFs and TAWIRFs for the training datasets in terms of the number of time lags [Eq. (35)]. The noise level of the wind stress and the 10% of mean eigenvalue of the wind stress autocovariance matrix are used as the regularization in the frequency domain WIRFs and the time domain WIRFs, respectively. The mean total residual variance ratios and the uncertainties (a shaded region is one standard deviation) are estimated from 30 realizations using the jackknife method.

estimated using the jackknife (Emery and Thomson 1998). The total residual variance ratios for the training data in the frequency and time domains are shown in Figs. 5a and 5b, respectively. The jackknife estimate for the impulse response function and its uncertainty are shown in the frequency domain for simplicity:

$$\mathbf{H}(\omega) = \frac{1}{M}\sum_{k=1}^{M}\left(\frac{\langle\hat{\mathbf{u}}\hat{\boldsymbol{\tau}}^{\dagger}\rangle}{\langle\hat{\boldsymbol{\tau}}\hat{\boldsymbol{\tau}}^{\dagger}\rangle}\right)_k, \tag{36}$$

$$\sigma^2_{\mathbf{H}(\omega)} = \frac{1}{M-1}\sum_{k=1}^{M}\left[\left(\frac{\langle\hat{\mathbf{u}}\hat{\boldsymbol{\tau}}^{\dagger}\rangle}{\langle\hat{\boldsymbol{\tau}}\hat{\boldsymbol{\tau}}^{\dagger}\rangle}\right)_k - \mathbf{H}(\omega)\right]^2, \tag{37}$$

where M is the number of subsampled datasets.

Cross validation (Efron and Gong 1983; LeBlanc and Tibshirani 1996) is repeated 30 times with randomly chosen blocks of training data and test data taking 90%

and 10% of the total data, respectively. The training data are chosen by subsampling with a uniform probability as opposed to a systematic choice of sequential contiguous blocks. Results of the two approaches (random or systematic) become nearly the same as the number of realizations increases, with little change in the results above 30 trials. In the frequency domain, the choice of the training data and test data is constrained because the data are divided into blocks with the same record length and are Fourier transformed separately. In the time domain, each excluded datum removes many lags. If they are distributed randomly, too many data are removed; therefore, they are subsampled in blocks. The regularization ($\mathbf{R_b}$) necessary to minimize the cross-validation error in the time domain WIRFs is about 10% of the mean eigenvalue (averaged variance) of the wind stress autocovariance matrix. On the other hand, the regularization in the frequency domain used a constant noise level, which decreases as the number of subsamples increases. The relationship between the error in the observations and the uncertainty in the WIRF estimate is discussed in section 5f.

The minimum number of subsamples and the maximum time lag are determined by the values at which the total cross-validated residual variance ratio averaged across all realizations (section 3c) is a minimum (Fig. 5). The number of subsamples is larger than the number of independent time series available from a given dataset. The 6-day chunks are assumed to be mostly independent, although the low-frequency components are not. The error bars on the WIRF and the residual variance are calculated using the jackknife method (see, e.g., Emery and Thomson 1998) with 30 randomly subsampled datasets [M is equal to 30 in Eqs. (36) and (37), and each subset is 90% of the total data].

The FIWIRF and FAWIRF are calculated from an ensemble of 90 independent FFTs of an 8.12-day period of the surface current and wind stress [section 3a(1) and Eq. (28)], and the TIWIRF and TAWIRF are computed from the wind stress stacked with hourly time lags up to six days regressed on the surface current [section 3a(2) and Eq. (29)]. These are approximately the minima of the cross-validated error (Fig. 5). The estimated WIRFs include the current response to steady wind ($\omega = 0$).

The WIRFs in one domain are (inversely) Fourier transformed into the other domain, and each pair satisfies Parseval's theorem. For example, the estimated FIWIRF (Figs. 6a and 6b) is inversely Fourier transformed into the time domain to represent a temporal amplitude (Fig. 6c). The estimated TIWIRF (Fig. 12c) is Fourier transformed into the frequency domain (Figs. 12a and 12b), so that the FIWIRF and TIWIRF are comparable across the two domains, and a similar procedure can be

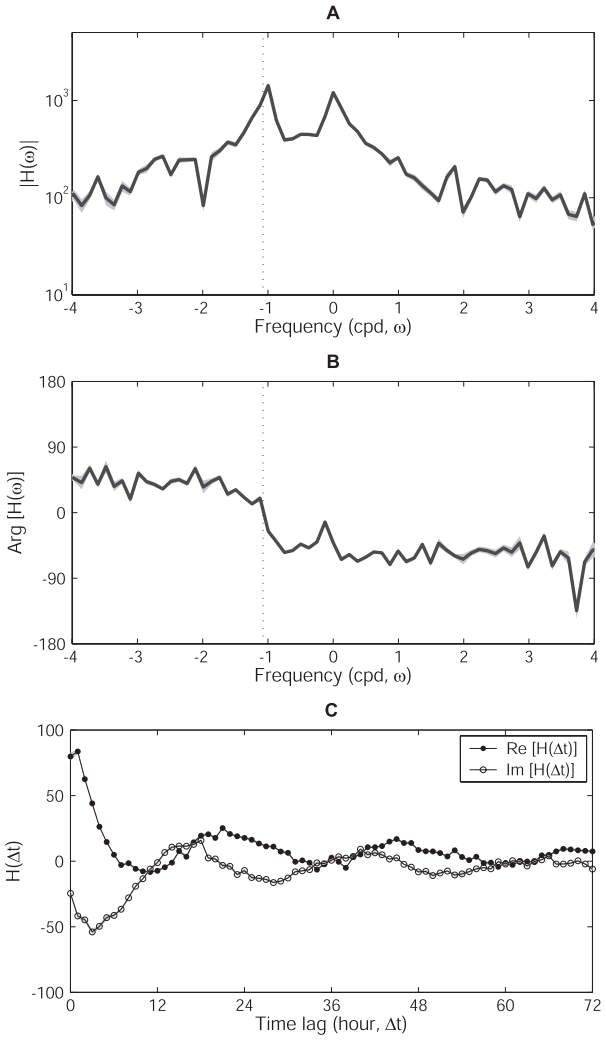

FIG. 6. (a) Magnitude, (b) phase, and (c) temporal amplitudes of the linearly estimated FIWIRF. The FIWIRF is estimated with 90 subsamples. The uncertainty shown as the gray-shaded region in (a) and (b) is calculated from 30 realizations using the jackknife method. The vertical dotted line indicates the inertial frequency ($\omega = -1.07$ cpd) in the study domain.

applied to the FAWIRF (Fig. 7) and TAWIRF (Fig. 13). For the nonlinear WIRFs, only the linear regression coefficients [$\mathbf{H_1}$ in Eq. (28) and $\mathbf{G_1}$ in Eq. (29)] are considered for the comparison between the two domains.

The isotropic and anisotropic WIRFs are compared both as the rotary power spectra in the frequency domain and as the time-integrated response. For instance, the linear FIWIRF is plotted for only onshore wind (τ_x) because it is isotropic, but the linear FAWIRF is plotted for onshore and upcoast winds (τ_x and τ_y), respectively, as magnitude and phase in the frequency domain (Figs. 8a and 8b, respectively). The time integration of temporal amplitudes of the FIWIRF (Fig. 6c) and FAWIRF (Fig. 7c) for steady wind are compared (Fig. 9a). The

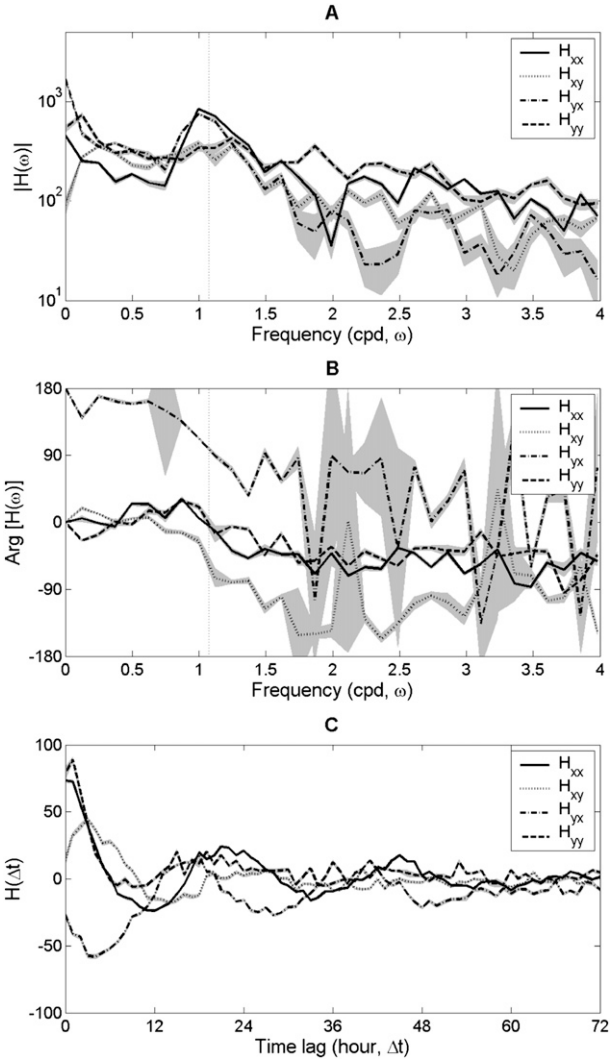

FIG. 7. Same as Fig. 6, but for the FAWIRF. The FAWIRF and its error bars are estimated in the same way as the FIWIRF (Fig. 6).

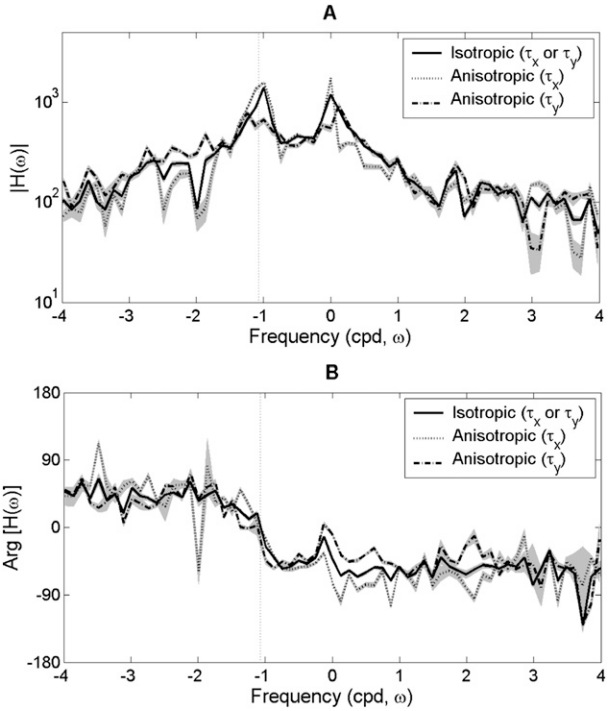

FIG. 8. (a) Magnitude and (b) phase of the linearly estimated FIWIRF and FAWIRF for wind stress (τ_x and τ_y), respectively. The phase of the FAWIRF for τ_y is shifted down by 90° to align with the others. The solid curves in (a) and (b) are the same as in Figs. 6a and 6b, respectively. See Fig. 6 for the definition of the vertical dotted line.

TIWIRF and TAWIRF are also examined in the similar way (Fig. 9b). The anisotropic response to upcoast wind is shifted 90° down (Figs. 8b and 14b) and rotated 90° clockwise (Fig. 9) to align with the other results. Moreover, the nonlinear anisotropic WIRFs are illustrated for steady winds with four directions: onshore ($\tau_x > 0$), offshore ($\tau_x < 0$), upcoast ($\tau_y > 0$), and downcoast ($\tau_y < 0$) winds.

Because of the ambiguity of WIRFs with tides at the S_2 frequency, the linear WIRFs estimated with the surface current both including and excluding the S_2 variance are compared. With the S_2 variance included in the fit, the residual variance ratios of the WIRF at the S_2 frequency is approximately 0.48, but the contribution of the S_2 variance to the total variance is negligible. The WIRFs with and without the S_2 variance overlap within error bars and the S_2 variance of the wind is small, so the surface current excluding the S_2 variance is used. The variance removal at the S_2 frequency is particularly evident in the plots of WIRFs (Figs. 8a and 14a) as a drop in the response function at that frequency.

b. Linear WIRFs

1) FREQUENCY DOMAIN

The magnitudes of the FIWIRF and FAWIRF have peaks near the diurnal frequency ($\omega = -1$ cpd for the FIWIRF and $\omega = 1$ cpd for the FAWIRF) instead of the Coriolis frequency ($\omega = \pm f_c$), as shown in Figs. 6a and 7a. Because the variances of the diurnal surface currents and diurnal wind stress are much larger than those at the Coriolis frequency, the WIRFs do not have as good signal-to-noise-ratio (SNR) at the Coriolis frequency, and the regularized least squares estimate biases the response function toward zero so that the estimated FIWIRF and FAWIRF have a maximum at the diurnal frequency ($\omega = -1$ and $\omega = 1$ cpd, respectively). There is also increasing uncertainty at higher frequency as a result of the dominance of the diurnal variance in the data (Figs. 6a and 7a).

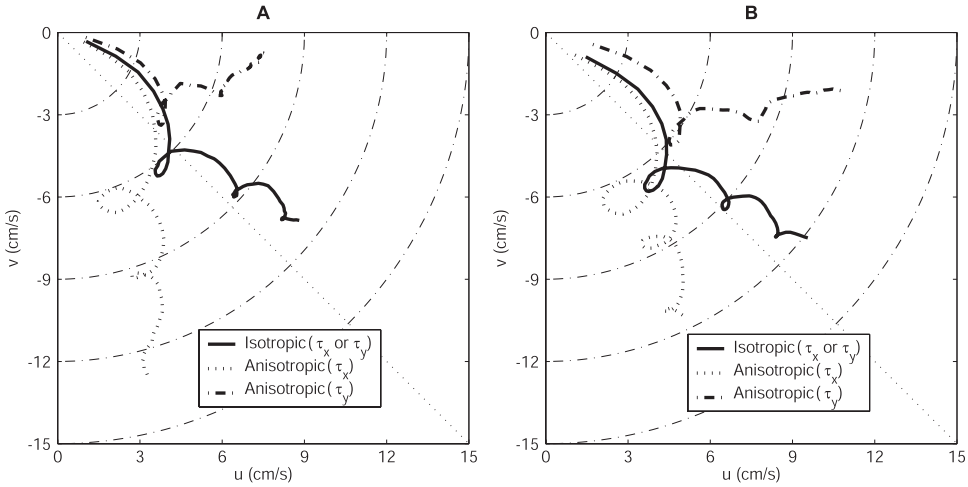

FIG. 9. Time integrations of the temporal amplitudes of the linearly estimated WIRFs for a constant wind stress during three days for (a) FIWIRF and FAWIRF and (b) TIWIRF and TAWIRF. The wind stress at either direction of the typical wind speed ($|\mathbf{u}| = 3$ m s^{-1}) in the study domain is applied. Anisotropic response for τ_y is rotated 90° clockwise to align with other responses. The thin dashed–dotted quarter-circular curves denote the percentage of the wind-driven current speed to the wind speed, which are 1%, 2%, 3%, 4%, and 5% from the origin, and the thin dotted line indicates the direction of 45° to the right of the wind stress.

The phase of the FIWIRF is nearly zero at $\omega \cong -f_c$, and varies between $-45°$ and 45° (Fig. 6b). The overall shapes of the FIWIRF (Figs. 6a and 6b) agree with the FIWIRF at the ocean surface of the Ekman theory (Figs. 1a and 1c) and as seen in other observations (Gonella 1972; Weller 1981; Rio and Hernandez 2003). The temporal amplitude of the FIWIRF has diurnal fluctuations and diminishes within 3–4 days with a clockwise rotation (Fig. 6c). This time-decaying amplitude is different from the evanescent solution for the step-function wind using the Laplace transform (Ekman 1905; Lewis and Belcher 2004), because we measure a local response for a statistically steady-state wind in the coastal region.

The FAWIRF is made up of four response functions, which gives twice the number of parameters as the FIWIRF. The cross terms (H_{xy} and H_{yx}) have more uncertainties in their magnitudes and phases than the diagonal terms (H_{xx} and H_{yy}; Figs. 7a and 7c). At $\omega = 0$, the phases of the FAWIRF are the same as the phases of the Ekman theory (Figs. 7b and 1d). However, the magnitudes of four terms (H_{xx}, H_{xy}, H_{yx}, and H_{yy}) of the FAWIRF at $\omega = 0$ are not identical as they were in the isotropic case showing anisotropic response in the quasi-steady state (Figs. 7a and 1b). The wind-current responses at all other frequencies are anisotropic, although noise in the estimate certainly contributes. The viscosity (ν) and adjustment terms (a_{xx}, a_{xy}, a_{yx}, and a_{yy}) could be estimated as functions of frequency using the observations, and an example of the fit of adjustment terms to the data is presented in appendix B. The temporal amplitude of the FAWIRF has approximately inertial periodicity and decays to zero within 3–4 days (Fig. 7c).

Coherence calculations (not shown) find that 60%–70% of the variances of the diurnal surface currents are explained by the diurnal land/sea breezes [Eqs. (31) and (32)]. However, the y-directional surface current (v) in the low-frequency band ($0 \leq \omega < 1$ cpd) has higher coherence with wind than the x-directional surface current (u) ($\beta_v^2 \approx 0.5$ and $\beta_u^2 \approx 0.3$). This is consistent with the hypothesis that the coastline in the study domain blocks flow to the east so that positive u is inhibited by the pressure setup at long time scales.

The FAWIRF to each wind component (τ_x or τ_y) is compared with the FIWIRF as rotary spectra (Fig. 8). Here τ_x apparently generates a stronger response at both clockwise diurnal frequency and zero frequency than τ_y (Fig. 8a), partly because of higher SNR. The phases of the FAWIRF for τ_x and τ_y vary between $-45°$ and 45° and bracket the phase of the FIWIRF (Fig. 8b) as the extended Ekman theory does (Fig. 2d). As an example, the temporal amplitudes of the FIWIRF and FAWIRF are integrated for three days under constant wind stress (0.013 kg m^{-1} s^{-2} for the typical wind speed in the study domain of 3 m s^{-1}), as shown in Fig. 9a. The FIWIRF generates surface currents 41° ± 2° to the right of steady wind, and the FAWIRF produces surface currents at 75° ± 0.5° (τ_x) and 9° ± 2° (τ_y) to the right of the steady wind stress, respectively, which are identical of the phases at $\omega = 0$ in Fig. 8b. The time integration of

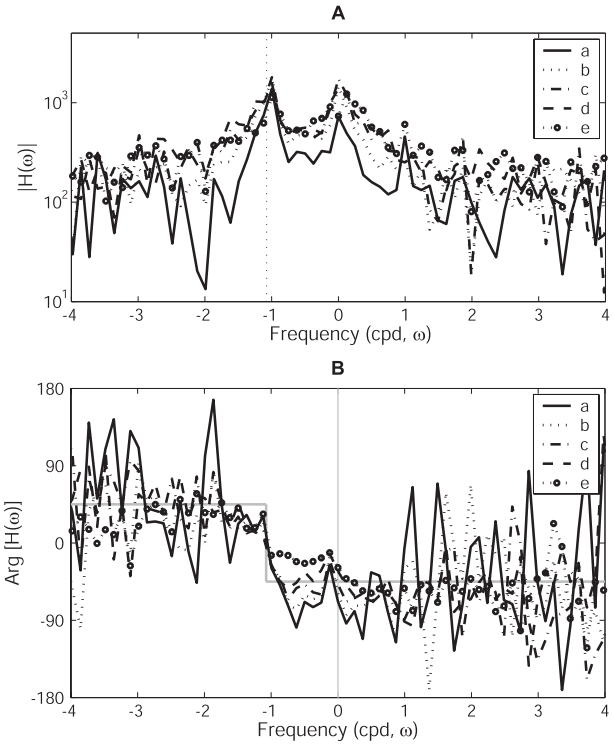

FIG. 10. (a) Magnitude and (b) phase of the FIWIRF in the cross-shelf direction. The gray line in (b) denotes the theoretical phase of the FIWIRF in the study domain. See Fig. 6 for the definition of the vertical dotted line.

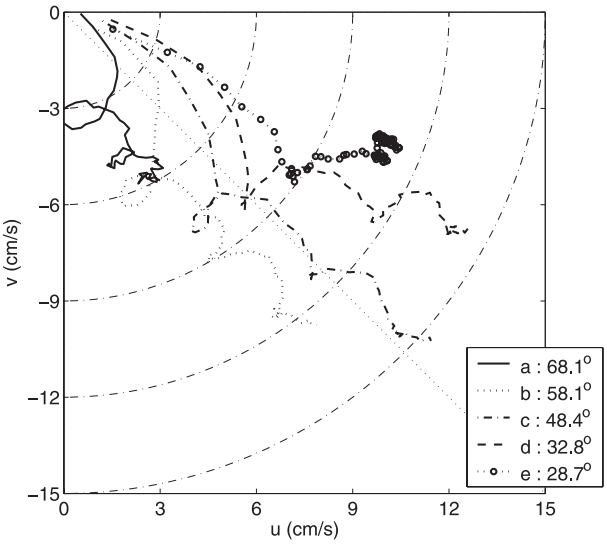

FIG. 11. Time integration of the temporal amplitude of the FIWIRF in the cross-shelf direction [(a) offshore and (e) onshore locations] for a constant wind stress during three days. Here τ_x of the typical wind speed ($|u| = 3$ m s^{-1}) in the study domain is applied. The veering angles from offshore to onshore are 68.1°, 58.1°, 48.4°, 32.8°, and 28.7° to the right of the steady wind. See Fig. 9 for the definitions of the curves and lines.

the steady wind response shows that the response is smaller cross-shore than alongshore, as expected. The magnitudes of the wind-driven currents are 3%–5% of the wind speed, which is consistent with other studies (Bye 1965; Churchill and Csanady 1983; Wu 1983; Weber 1983). The total residual variance ratios by the FIWIRF and FAWIRF are 0.62 and 0.52, respectively (Fig. 5a), indicating significant anisotropy.

The spatial variation of WIRFs is examined by computing the FIWIRF between the detided surface currents at five locations sampling the cross-shelf direction in the study domain (grid points a−e in Fig. 3) and wind stress. Each FIWIRF is made from 90 subsamples with the same record length and averaged over the realizations at each frequency. As an example of cross-shelf variation of WIRFs, the magnitude and phase of the FIWIRF at five evenly spaced points sampling the cross-shelf direction are shown in Fig. 10a and 10b, respectively. The FIWIRF shows larger response onshore than offshore. To show the response to a steady wind, the temporal amplitude of the FIWIRF is integrated in time for three days with a constant typical wind speed in San Diego (Fig. 11). As the point considered moves from offshore to onshore, the veering angle changes from 70° (offshore) to 30° (onshore) to the right of the wind. The slower rotation with depth inshore may imply the less of full Ekman layer may be fit into the shallow water depth (Ekman 1905; Lentz 2001; Kirincich et al. 2005).

2) TIME DOMAIN

The TIWIRF and TAWIRF are shown in Figs. 12c and 13c , respectively, and the magnitude and phase of Fourier transformed TIWIRF and TAWIRF are shown in Figs. 12a and 12b and Figs. 13a and 13b, respectively. The TIWIRF shows approximately inertial oscillations with slowly decreasing amplitude (Fig. 12c), which are slightly larger than that of the FIWIRF (Fig. 6c). However, the energy of the TIWIRF and the FIWIRF is nearly equal when the time lag and the data record length are same. The energy of the TAWIRF and the FAWIRF is also approximately the same within the estimation errors. The SNR of the TAWIRF is again relatively lower at the Coriolis frequency than at the diurnal frequency, so the peaks are found close to 1 cpd.

The magnitude of the TIWIRF in the frequency domain is large at the diurnal frequency (Fig. 12a), and its phase stays between −45° and 45° with phase shift of nearly zero degree at $\omega \cong -f_c$ (Fig. 12b). The phase of the TIWIRF at zero frequency is −43° ± 2° (Fig. 6b or 14b), which is consistent with the phase of the FIWIRF

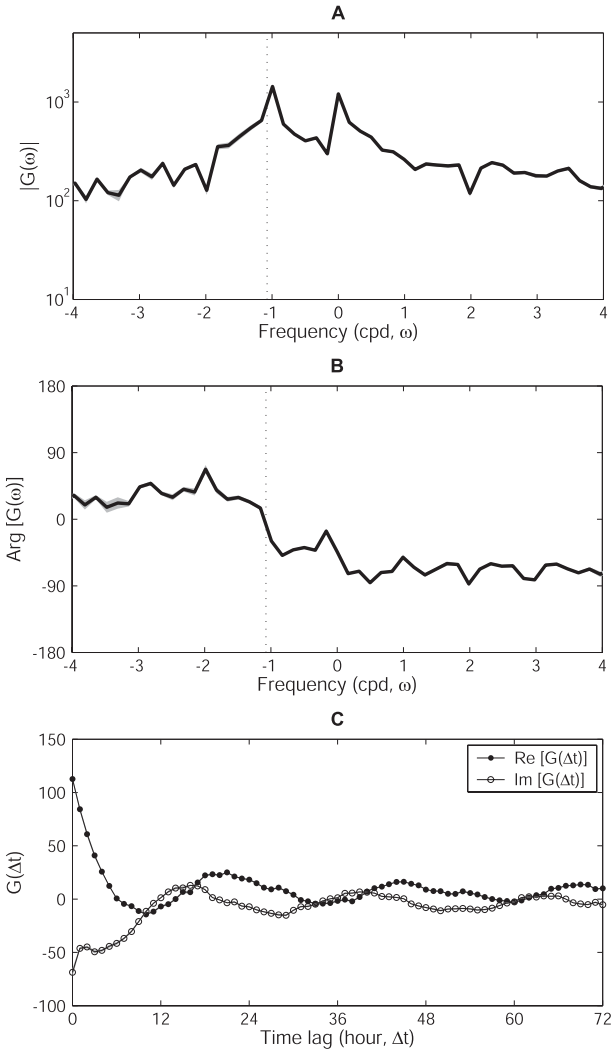

FIG. 12. (a) Magnitude and (b) phase of the inversely Fourier transformed TIWIRF, and (c) amplitude for the linearly estimated TIWIRF. The TIWIRF is estimated with the surface currents and 6-day timelag stacked wind stress. The uncertainty is calculated from 30 realizations using the jackknife method. See Fig. 6 for definition of the vertical dotted line.

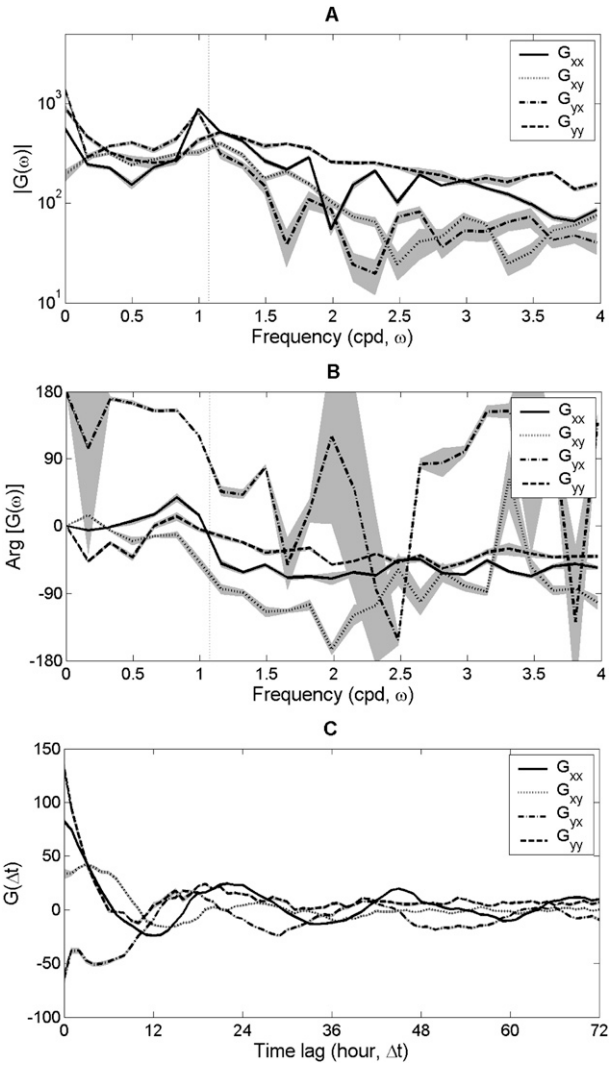

FIG. 13. Same as Fig. 12 but the linearly estimated TAWIRF. The TAWIRF and its error bar are estimated in the same way as the TIWIRF (Fig. 12). See Fig. 6 for definition of the vertical dotted line.

(−41° ± 2°, Fig. 8b). The TAWIRF (Fig. 13) has similar features to the FAWIRF (Fig. 7).

The Fourier transformed TIWIRF and TAWIRF for each wind component (τ_x and τ_y) are compared as rotary spectra (Fig. 14) and also show the peak at the diurnal frequency, the drops at the S_2 frequency, and the bracketing phases of the TAWIRF as with the frequency domain WIRFs.

The time-integrated responses (Fig. 9b) of the TIWIRF and TAWIRF to typical constant wind stress in the study domain also show similar patterns to those of the FIWIRF and FAWIRF (Fig. 9a). In a quasi-steady state, the TAWIRF generates surface current responses of 67° ± 1° (τ_x) and 12° ± 3° (τ_y) to the right of the wind stress, respectively, and the TIWIRF yields surface currents at 43° ± 2° to the right of the wind direction. The suppression of the cross-shore response is still evident because the veering angle of the response rotates the current away from the cross-shore direction when compared to the isotropic response. The fraction of surface current variance explained by the TIWIRF and TAWIRF with 6-day time lag is 43.9% and 54.7% of the total current variance, respectively (Fig. 5b).

Although the linear WIRFs show anisotropy in the wind response, the responses to onshore and offshore winds (or upcoast and downcoast winds) are identical.

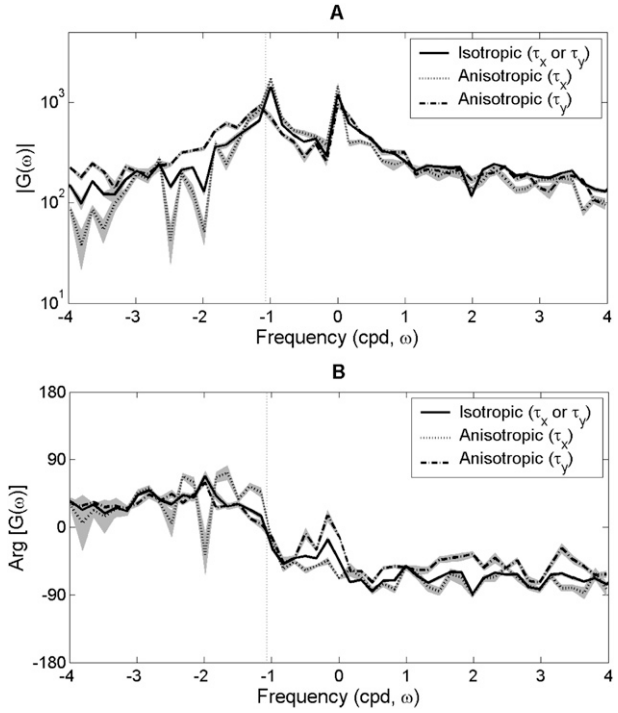

FIG. 14. Same as Fig. 8, but for TIWIRF and TAWIRF. The phase of the TAWIRF for τ_y is shifted down 90° to align with others. The solid curves in (a) and (b) are the same in Figs. 12a and 12b, respectively. See Fig. 6 for the definition of the vertical dotted line.

c. Nonlinear WIRFs

The magnitude and phase of the WIRF (**G** or **H**) in the linear regression are similar to those of the linear part ($\mathbf{G_1}$ or $\mathbf{H_1}$, respectively) in the nonlinear regression (not shown). The nonlinear term ($\mathbf{G_2}$ or $\mathbf{H_2}$) controls the asymmetric current response. However, their contributions cannot be simply presented in the form of the linearly estimated WIRFs (e.g., magnitude and phase in Figs. 8 and 14) because of nonlinearity.

The time integrations of the temporal amplitudes of the linear and nonlinear WIRFs are shown in Fig. 15 to examine the anisotropic and asymmetric responses to four different steady winds. Whereas the linear FIWIRF (Fig. 15a) has an isotropic response, the nonlinear FIWIRF shows a different response to onshore and offshore winds. The response of the nonlinear FIWIRF to onshore wind is closer to alongcoast compared to the onshore wind response of the linear FIWIRF, and the offshore wind generates a much stronger response at about 40° to the right of the wind direction. Because of the isotropy assumption, the response of the nonlinear FIWIRF to the upcoast wind is identical to that to the onshore wind and the same for the offshore wind and downcoast wind.

The time-integrated responses of the linear and nonlinear FAWIRFs are shown in Figs. 15b and 15c, respectively. The response of the linear FAWIRF was discussed in Fig. 9a, but it is plotted with all four quadrants for easier comparison to the nonlinear results, with the current suppressed in the onshore direction and enhanced in the offshore direction (Fig. 15b). The response of the nonlinear FAWIRF shows asymmetric features in the coastal region (Fig. 15c).

The time-integrated responses of the linear/nonlinear TIWIRFs and TAWIRFs are shown in Figs. 15d–15f, and those have nearly the same pattern as the frequency domain WIRFs.

d. Wind-driven surface circulation

One of the benefits of the WIRF is to provide a complete description of the wind-driven flow. The complexity of the wind-driven surface current was examined (not shown) using the nonlinear FAWIRF and two wind cases: constant wind and diurnal wind (hourly composite mean wind stress). The responses to the steady wind from multiple directions (not shown) reflect coastline and bathymetry effects. The surface current response to the onshore wind is inhibited by coastline and veers either upcoast or downcoast. The response to the downcoast wind within 160°–240° (in clockwise from true north) is 30%–40% stronger than response to the wind in other directions. The diurnal wind generates rotating currents with the elliptical or skewed responses by the coastline, with different phases (not shown) resulting from varying time lags.

e. Residual variance ratio

The total residual variance ratio of the nonlinearly estimated WIRFs plotted against the number of subsamples (Fig. 5a for the FIWIRF and FAWIRF) and the number of time lags (Fig. 5b for the TIWIRF and TAWIRF) show improvement over the linear fits. Compared with the linear estimate, the total residual ratio is reduced by about 5% in the frequency domain estimates (FIWIRF and FAWIRF) and by about 4% for the time domain estimates (TIWIRF and TAWIRF). This is not significant beyond one standard deviation, but it is greater than that expected for adding red noise parameters and the physical results are sensible (Fig. 15).

f. Errors in the WIRF

The error in the estimated WIRF can result from several sources: the measurement errors of surface currents and wind, statistical uncertainty, and errors introduced by the parameterization of the WIRF. The

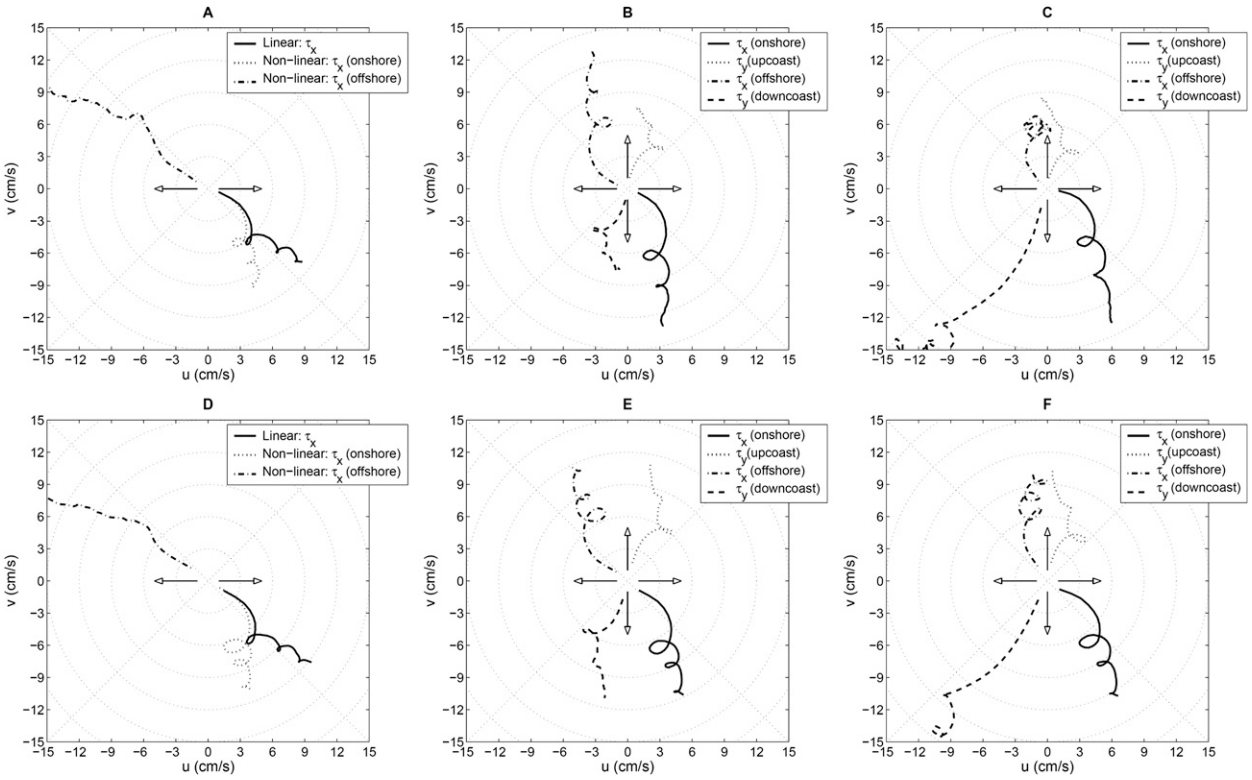

FIG. 15. (top) Time integrations of the temporal amplitudes of the frequency domain WIRFs for a constant wind stress during three days for (a) linear FIWIRF ($\hat{\mathbf{u}} = \mathbf{H}\hat{\boldsymbol{\tau}}$) and nonlinear FIWIRF ($\hat{\mathbf{u}} = \mathbf{H_1}\hat{\boldsymbol{\tau}} + \mathbf{H_2}|\hat{\boldsymbol{\tau}}|$); (b) linear FAWIRF, which is a four quadrant plot of Fig. 9a; and (c) nonlinear FAWIRF. (bottom) Time integrations of the time domain WIRFs for a constant wind stress during three days for (d) linear TIWIRF ($\mathbf{u} = \mathbf{G}\boldsymbol{\tau}_N$) and nonlinear TIWIRF ($\mathbf{u} = \mathbf{G_1}\boldsymbol{\tau}_N + \mathbf{G_2}|\boldsymbol{\tau}_N|$); (e) linear TAWIRF, which is a four quadrant plot of Fig. 9b; and (f) nonlinear TAWIRF. The constant wind stress is presented as an arrow for each direction: up (upcoast), down (downcoast), right (onshore), and left (offshore). See Fig. 9 for the definitions of the curves and lines.

measurement error of surface currents in the study domain is about 5.5 cm s^{-1} (Kim et al. 2008) and is assumed to be uncorrelated in time, so that averaging over many realizations reduces the effects of this error. The wind measurement error is reported as ±2% of the wind speed (0.04–0.18 m s^{-1}). The statistical uncertainty is estimated using the jackknife method but that does not completely characterize the error. Least squares methods include error estimates, which account for missing information.

The contamination of the observed currents by the measurement noise and other processes is modeled by a white noise spectrum used to calculate a SNR at each frequency. The estimated linear frequency domain WIRF [Eq. (23)] can be rewritten as

$$\mathbf{H} = (\hat{\boldsymbol{\tau}}^\dagger \mathbf{R}_\mathbf{a}^{-1} \hat{\boldsymbol{\tau}} + \mathbf{P}^{-1})^{-1} \hat{\boldsymbol{\tau}}^\dagger \mathbf{R}_\mathbf{a}^{-1} \hat{\mathbf{u}} \tag{38}$$

$$= (\hat{\boldsymbol{\tau}}^\dagger \hat{\boldsymbol{\tau}} + \mathbf{P}^{-1}\kappa^2)^{-1} \hat{\boldsymbol{\tau}}^\dagger \hat{\mathbf{u}}, \tag{39}$$

where $\mathbf{R_a} = \kappa^2\mathbf{I}$ is the noise level assumed as a constant, and $\mathbf{P}$ is the prior uncertainty of the WIRF.

The posterior uncertainty covariance ($\hat{\mathbf{P}}$) of the WIRF is

$$\hat{\mathbf{P}} = (\hat{\boldsymbol{\tau}}^\dagger \mathbf{R}_\mathbf{a}^{-1} \hat{\boldsymbol{\tau}} + \mathbf{P}^{-1})^{-1} = \kappa^2 (\hat{\boldsymbol{\tau}}^\dagger \hat{\boldsymbol{\tau}} + \mathbf{P}^{-1}\kappa^2)^{-1}. \tag{40}$$

The amplitude of the uncertainty is somewhat arbitrary, because the choice of a white noise spectrum is oversimplified and poorly constrained, but the posterior uncertainty (not shown) has larger errors away from the frequencies with strong driving.

This error analysis does not account for systematic errors in the wind or current measurements. The errors in the wind measurements translate to model errors in the regression, so that the problem becomes deconvolution for solutions by total least squares (Golub and van Loan 1980; van Huffel and Vandewalle 1991) or other methods, which are outside the scope of this work.

6. Discussion and conclusions

Wind impulse response functions are statistically estimated from spatially averaged observed surface

currents and shore station wind in both frequency and time domains to examine anisotropic and nonlinear current response in the coastal area. The surface current response due to coastal wind forcing is found to be anisotropic—that is, dependent on wind direction—in contrast to the isotropic response in the open ocean. Bottom and coastline boundaries including islands and headlands support local sea level gradients due to wind and may also yield anisotropic bottom drag. For steady wind forcing for three days, the linear isotropic current response estimated in the frequency or time domain is $42° \pm 2°$ to the right of wind direction, regardless of the wind direction. However, the linear anisotropic current response in both domains is $10° \pm 4°$ to the right of the upcoast wind and $71° \pm 3°$ to the right of the onshore wind. The linearly estimated FAWIRF and TAWIRF by construction produce the same response to onshore and offshore winds (or upcoast and downcoast winds). Only the nonlinear WIRFs can show asymmetric current response. The surface current response discussed in this paper includes the wind-driven components coupled with the bottom and depth effects.

The instantaneous acceleration of the current is proportional to wind stress, friction, and pressure gradients. The direct correlation of the wind stress and the acceleration of surface currents ($\partial \mathbf{u}/\partial t$) are relatively low as a result of noise in the derivatives. Instead of the momentum balance, the regression is used, which implies time integration of the momentum equations. The response to the wind includes sea surface set up because of the cumulative effects of currents interacting with topography. Thus the wind response we consider here can include currents accelerated by the pressure gradients because of sea surface set up, as considered by Ekman (1905). The anisotropy of the coastline and bathymetry leads to an anisotropic response of the currents through pressure set up and frictional effects.

For the comparison of estimated WIRFs, the total residual variance ratio is calculated by cross validation for the training data, and the uncertainty is estimated using the jackknife method. The regularization in the frequency and time domain WIRF estimates is picked to optimize the cross-validation performance. The error bars of the isotropic and anisotropic WIRFs do not overlap, so the improvement in fitting attained by allowing anisotropy is robust.

The advantages in the use of spatially averaged surface currents are to avoid the ambiguity in the spatial decorrelation of both surface currents and wind stress, to increase the SNR in the surface currents with less missing data, and to provide a representative view of the study domain. In addition, the effects of missing data are potentially represented in the error bars calculated by the jackknife method. Missing data are less of a problem for the time domain calculation of the WIRF because the correlation uses only the data available without either interpolation or zero filling. This comes at the expense of nonpositive-definite covariance matrices, and the crude regularization we apply may affect the results. Similar results for both frequency and time domains estimates show that missing data are not a dominant effect.

Although the data and methodology presented document the anisotropic wind response of the ocean near San Diego, it is noteworthy to emphasize that the response is a combination of both directly wind-driven flow and alongshore geostrophic response to upwelling/downwelling favorable winds. Given the site specific nature of the latter dynamics, a logical extension of this work would be a broad area examination of the response function along the U.S. West Coast, taking advantage of the growing HF radar-mapped surface currents records. It is expected that the spatially varying U.S. West Coast wind climate, coupled with a complex coastline geometry, will introduce gradients in the geostrophic response that can be diagnosed in those datasets using the wind impulse response functions described in this paper.

The anisotropic wind response in coastal waters has broad-ranging implications to the understanding and prediction of the transport of biologics, contaminants, spilled oil, and other waterborne constituents in the coastal zone, especially for those scenarios where ''rule of thumb'' estimates of wind drift are used for predicting the Lagrangian behavior of the upper ocean. This is especially prevalent in operational communities dealing with oil spills and search/rescue response. In addition, anisotropic surface current response suggests that coastal upwelling indices and estimates based upon wind climatology may have biases that need further investigation. The previously mentioned study would be a first step in this direction and would assist in growing interests in including ocean dynamics in simple coastal productivity models and fisheries research.

Acknowledgments. Sung Yong Kim is supported by the Coastal Ocean Currents Monitoring Program (COCMP) from the State of California and the Office of Naval Research (ONR). Bruce Cornuelle is sponsored by both NOAA (NOAA Grant NA17RJ1231) and COCMP. Eric Terrill is supported through funding provided by the ONR, COCMP, and NOAA. Surface current data are provided from the Southern California Coastal Ocean Observing System (SCCOOS; available online at http://www.sccoos.org) at Scripps Institution of Oceanography (SIO), and wind data at Tijuana River (Tidal Linkage) are maintained

by the System-Wide Monitoring Program at the Tijuana River National Estuarine Research Reserve (TRNERR), Estuarine Reserves Division, NOAA, Centralized Data Management Office (CDMO; available online at http://cdmo.baruch.sc.edu/), Baruch Marine Field Lab, and the University of South Carolina. We thank M. Otero, L. Hazard, P. Reuter, J. Bowen, and T. Cook in Coastal Observing Research and Development Center (CORDC; available online at http://cordc.ucsd.edu/) at SIO, and M. Ide, M. Cordrey, and J. Crook at TRNERR.

APPENDIX A

WIRFs in Ekman Theory

Ekman theory at finite depth considered in the frequency domain

a. Isotropic approach

The momentum equations with depth-independent viscosity in physical space,

$$\frac{\partial u}{\partial t} - f_c v + a_{xx} * u = \nu \frac{\partial^2 u}{\partial z^2}, \tag{A1}$$

$$\frac{\partial v}{\partial t} + f_c u + a_{yy} * v = \nu \frac{\partial^2 v}{\partial z^2}, \tag{A2}$$

are combined and Fourier transformed into the frequency domain assuming an isotropic friction coefficient ($a_{xx} = a_{yy} = r\delta(t)$ and $a_{xy} = a_{yx} = 0$):

$$\lambda^2 \hat{\mathbf{u}}(z,\omega) = \frac{\partial^2 \hat{\mathbf{u}}(z,\omega)}{\partial z^2}, \tag{A3}$$

where $\lambda = \sqrt{[i(\omega + f_c) + r]/\nu}$. $\hat{\boldsymbol{\tau}}(\omega)$ and $\hat{\mathbf{u}}(z,\omega)$ denote the wind stress and currents in the frequency domain. When boundary conditions at the surface ($z = 0$) and finite depth ($z = -h$) are applied, the upper boundary condition sets viscous stress equal to wind stress,

$$\left.\frac{\partial \hat{\mathbf{u}}(z,\omega)}{\partial z}\right|_{z=0} = \frac{\hat{\boldsymbol{\tau}}(\omega)}{\rho\nu}. \tag{A4}$$

If the lower boundary condition sets flow to zero,

$$\hat{\mathbf{u}}(z,\omega)|_{z=-h} = 0, \tag{A5}$$

the FIWIRF is

$$\mathbf{H}(z,\omega) = \frac{\hat{\mathbf{u}}(z,\omega)}{\hat{\boldsymbol{\tau}}(\omega)} = \frac{\sinh\lambda(z+h)}{\lambda\rho\nu\cosh(\lambda h)}. \tag{A6}$$

If the lower boundary condition enforces zero deep stress,

$$\left.\frac{\partial \hat{\mathbf{u}}(z,\omega)}{\partial z}\right|_{z=-h} = 0, \tag{A7}$$

the FIWIRF becomes

$$\mathbf{H}(z,\omega) = \frac{\hat{\mathbf{u}}(z,\omega)}{\hat{\boldsymbol{\tau}}(\omega)} = \frac{\cosh\lambda(z+h)}{\lambda\rho\nu\sinh(\lambda h)}, \tag{A8}$$

and its magnitude and phase are identical to Eq. (A6).

b. Anisotropic approach

The momentum equations in the frequency domain are

$$\alpha_{xx}\hat{u} + \alpha_{xy}\hat{v} = \nu\frac{\partial^2 \hat{u}}{\partial z^2}, \tag{A9}$$

$$\alpha_{yx}\hat{u} + \alpha_{yy}\hat{v} = \nu\frac{\partial^2 \hat{v}}{\partial z^2}, \tag{A10}$$

where $\alpha_{xx} = i\omega + a_{xx}$, $\alpha_{xy} = -f_c + a_{xy}$, $\alpha_{yx} = f_c + a_{yx}$, and $\alpha_{yy} = i\omega + a_{yy}$. When Eq. (A9) is used to solve for $\hat{v}(z,\omega)$,

$$\hat{v} = \frac{1}{\alpha_{xy}}[\nu\hat{u}^{(2)} - \alpha_{xx}\hat{u}], \tag{A11}$$

and substituted into Eq. (A10), the fourth-order ordinary differential equation results in

$$\nu^2\hat{u}^{(4)} - \nu(\alpha_{xx} + \alpha_{yy})\hat{u}^{(2)} + (\alpha_{xx}\alpha_{yy} - \alpha_{xy}\alpha_{yx})\hat{u} = 0, \tag{A12}$$

where $B^{(n)}$ is the nth order of derivative with respect to z. Assuming that the solution of Eq. (A12) is

$$\hat{u}(z,\omega) = \sum_{j=1}^{4} c_j(\omega)e^{\lambda_j(\omega)z}, \tag{A13}$$

this assumption works only when ν is depth independent. From the characteristic equation of Eq. (A12),

$$\hat{u}^{(4)} + p\hat{u}^{(2)} + q\hat{u}^{(1)} + s\hat{u} = 0, \tag{A14}$$

$$\lambda^4 + p\lambda^2 + q\lambda + s = 0, \tag{A15}$$

where $p = -(\alpha_{xx} + \alpha_{yy})/\nu$, $q = 0$, and $s = (\alpha_{xx}\alpha_{yy} - \alpha_{xy}\alpha_{yx})/\nu^2$. The quartic equation can be solved by Ferrari–Cardan's method (Smith 1959). An additional parameter (m) is introduced,

$$(\lambda^2 + p + m)^2 = (p + 2m)\lambda^2 + (p^2 - s + 2pm + m^2), \tag{A16}$$

and three m are found to satisfy that the determinant of the right-hand side of Eq. (A16) is equal to zero [$D = -4(p + 2m)(p^2 - s + 2pm + m^2) = 0$]:

$$m_1 = -\frac{p}{2} \quad \text{and} \quad m_{2,3} = -p \pm \sqrt{s}. \tag{A17}$$

For each m, four characteristic roots (λ) exist. When $m = -p/2$,

$$\lambda^2 = -\frac{p}{2} \pm \sqrt{\frac{p^2}{4} - s} \tag{A18}$$

$$= \frac{\alpha_{xx} + \alpha_{yy}}{2\nu} \pm \frac{1}{\nu}\sqrt{\frac{(\alpha_{xx} - \alpha_{yy})^2}{4} + \alpha_{xy}\alpha_{yx}}. \tag{A19}$$

When $m = -p \pm \sqrt{s}$,

$$\lambda_{1,2} = \frac{1}{2}\left(\sqrt{-p + 2\sqrt{s}} \pm \sqrt{-p - 2\sqrt{s}}\right), \tag{A20}$$

$$\lambda_{3,4} = \frac{1}{2}\left(\sqrt{-p - 2\sqrt{s}} \pm \sqrt{-p + 2\sqrt{s}}\right). \tag{A21}$$

The boundary conditions at the top (wind stress) and bottom (zero deep stress) are applied,

$$\left.\frac{\partial \hat{u}(z,\omega)}{\partial z}\right|_{z=0} = \frac{\hat{\tau}_x(\omega)}{\rho\nu}, \tag{A22}$$

$$\left.\frac{\partial \hat{v}(z,\omega)}{\partial z}\right|_{z=0} = \frac{\hat{\tau}_y(\omega)}{\rho\nu} \Rightarrow \frac{1}{\alpha_{xy}}(\nu\hat{u}^{(3)} - \alpha_{xx}\hat{u}^{(1)})\Big|_{z=0} = \frac{\hat{\tau}_y(\omega)}{\rho\nu}, \quad \text{and} \tag{A23}$$

$$\left.\frac{\partial \hat{u}(z,\omega)}{\partial z}\right|_{z=-h} = 0, \quad \text{and} \tag{A24}$$

$$\left.\frac{\partial \hat{v}(z,\omega)}{\partial z}\right|_{z=-h} = 0 \Rightarrow \frac{1}{\alpha_{xy}}(\nu\hat{u}^{(3)} - \alpha_{xx}\hat{u}^{(1)})\Big|_{z=-h} = 0. \tag{A25}$$

Equation (A12) can be solved as an inverse problem (Wunsch 1996),

$$\mathbf{Ac} = \mathbf{d}, \tag{A26}$$

where $\mathbf{c} = \begin{bmatrix} c_1 \\ c_2 \\ c_3 \\ c_4 \end{bmatrix}$, $\mathbf{d} = \begin{bmatrix} \frac{\hat{\tau}_x(\omega)}{\rho\nu} \\ \frac{\hat{\tau}_y(\omega)}{\rho\nu}\alpha_{xy} \\ 0 \\ 0 \end{bmatrix}$, and

$$\mathbf{A} = \begin{bmatrix} \lambda_1 & \lambda_2 & \lambda_3 & \lambda_4 \\ \nu\lambda_1^3 - \alpha_{xx}\lambda_1 & \nu\lambda_2^3 - \alpha_{xx}\lambda_2 & \nu\lambda_3^3 - \alpha_{xx}\lambda_3 & \nu\lambda_4^3 - \alpha_{xx}\lambda_4 \\ e^{-\lambda_1 h} & e^{-\lambda_2 h} & e^{-\lambda_3 h} & e^{-\lambda_4 h} \\ (\nu\lambda_1^3 - \alpha_{xx}\lambda_1)e^{-\lambda_1 h} & (\nu\lambda_2^3 - \alpha_{xx}\lambda_2)e^{-\lambda_2 h} & (\nu\lambda_3^3 - \alpha_{xx}\lambda_3)e^{-\lambda_3 h} & (\nu\lambda_4^3 - \alpha_{xx}\lambda_4)e^{-\lambda_4 h} \end{bmatrix}.$$

The anisotropic response functions in the x direction (H_{xx} and H_{xy}) are estimated by solving Eq. (A26) numerically at each finite frequency and substituting the model efficient (**c**) into Eq. (A13). Then, the anisotropic response functions in the y direction (H_{yx} and H_{yy}) are estimated from Eq. (A11). All FAWIRFs for three choices of m in Eq. (A17) show the identical magnitude and phase.

APPENDIX B

Estimate of Adjustment Terms

The parameters of the Ekman model, including kinematic viscosity (ν) and adjustment terms (a_{xx}, a_{xy}, a_{yx}, and a_{yy}), can be estimated from data-derived WIRFs. However, there are limitations in the estimate as a result of the errors in the estimated WIRFs. In addition, the transformation between the parameters and the WIRF is nonlinear and must be inverted iteratively. As the simplest case, constant adjustment terms and viscosity are varied to approximately fit the width and the magnitude of the peak at the Coriolis frequency. The peak of the WIRF near zero frequency is not predicted by the Ekman model and may indicate frequency-dependent adjustment terms and Ekman layer parameters. The magnitude of the model WIRF is scaled by a constant for a compensating shift in magnitude of the data-derived WIRFs, which provides a clue for the viscosity estimate. The magnitude and phase of the

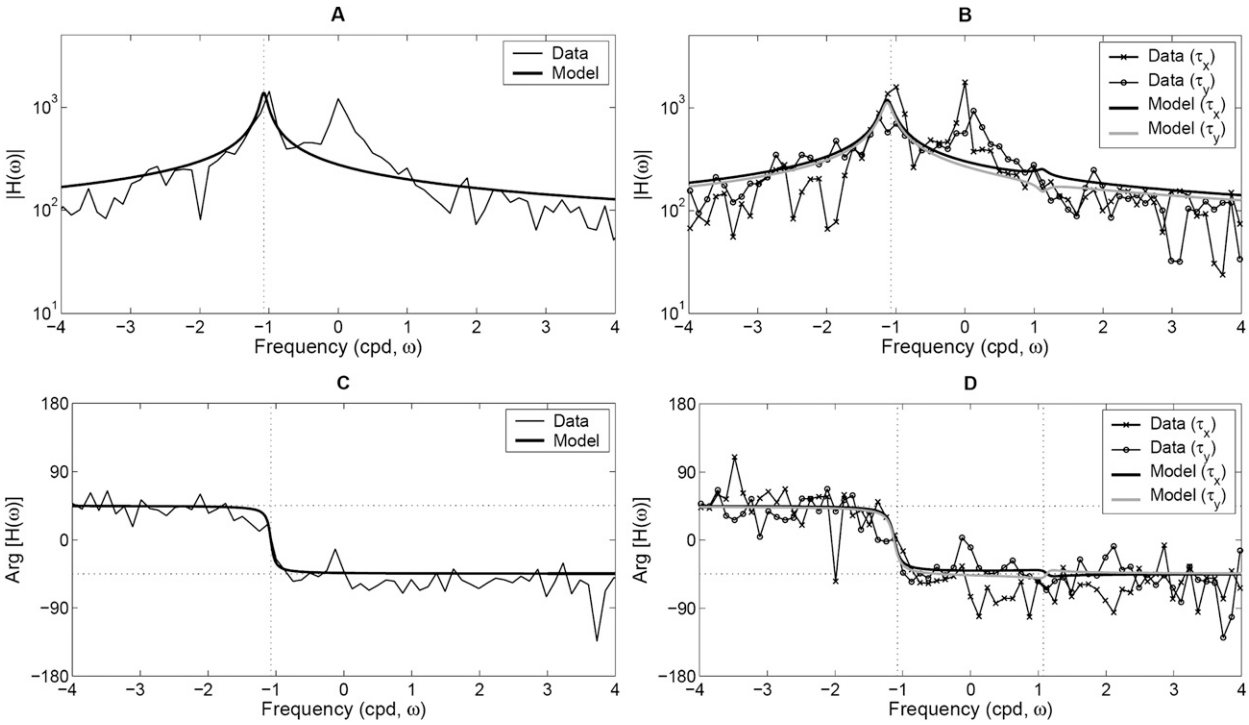

FIG. B1. Comparison of the model WIRF (thick line) and the data-derived WIRF (thin line): (a) magnitude and (c) phase of the FIWIRF ($r = 3.16 \times 10^{-6}\ s^{-1}$) and (b) magnitude and (d) phase of the FAWIRF ($r_{xx} = 1 \times 10^{-9}\ s^{-1}$, $r_{xy} = -8 \times 10^{-6}\ s^{-1}$, $r_{yx} = 0$, and $r_{yy} = 1 \times 10^{-5}\ s^{-1}$). The estimated viscosity (ν) is $2.1 \times 10^{-5}\ m^2\ s^{-1}$ in both FIWIRF and FAWIRF. See Fig. 6 for definition of the vertical dotted line.

FIWIRF and the model fit are shown in Figs. B1a and B1c, respectively. The estimated viscosity is $2.1 \times 10^{-5}\ m^2\ s^{-1}$ in both FIWIRF and FAWIRF and is within the typical viscosity range (section 2b). The isotropic friction coefficient (r) is equal to $3.16 \times 10^{-6}\ s^{-1}$. The anisotropic adjustment terms based on the data-derived FAWIRF are $r_{xx} = 1 \times 10^{-9}\ s^{-1}$, $r_{xy} = -8 \times 10^{-6}\ s^{-1}$, $r_{yx} = 0$, and $r_{yy} = 1 \times 10^{-5}\ s^{-1}$ (Figs. B1b and B1d). Although the adjustment terms can be a function of frequency, this is beyond the scope of this paper.

REFERENCES

Allen, J. S., 1980: Models of wind-driven currents on the continental shelf. *Annu. Rev. Fluid Mech.,* **12,** 389–433.

Alpers, W., 1985: Theory of radar imaging of internal waves. *Nature,* **314,** 245–247.

Barrick, D. E., M. W. Evans, and B. L. Webber, 1977: Ocean surface currents mapped by radar. *Science,* **198,** 138–144.

Beardsley, R. C., C. E. Dorman, C. A. Friehe, L. K. Rosenfeld, and C. D. Winant, 1987: Local atmospheric forcing during the coastal ocean dynamics experiment. 1: A description of the marine boundary layer and atmospheric conditions over a northern California upwelling region. *J. Geophys. Res.,* **92,** 1467–1488.

Bendat, J., and A. G. Piersol, 2000: *Random Data Analysis and Measurement Procedures*. 3rd ed. John Wiley & Sons, 594 pp.

Blackford, B. L., 1978: Wind-driven inertial currents in the Magdalen Shallows, Gulf of St. Lawrence. *J. Phys. Oceanogr.,* **8,** 653–664.

Bye, J. A. T., 1965: Wind-driven circulation in unstratified lakes. *Limnol. Oceanogr.,* **10,** 451–458.

Chereskin, T. K., 1995: Direct evidence for an Ekman balance in the California Current. *J. Geophys. Res.,* **100** (C9), 18 261–18 269.

Choi, B.-J., and J. L. Wilkin, 2007: The effect of wind on the dispersal of the Hudson River plume. *J. Phys. Oceanogr.,* **37,** 1878–1897.

Churchill, J. H., and G. T. Csanady, 1983: Near-surface measurements of quasi-Lagrangian velocities in open water. *J. Phys. Oceanogr.,* **13,** 1669–1680.

Davis, R. E., 1985: Objective mapping by least squares fitting. *J. Geophys. Res.,* **90** (C7), 4773–4777.

Efron, B., and G. Gong, 1983: A leisurely look at the bootstrap, the jackknife, and the cross-validation. *Amer. Stat.,* **37,** 36–48.

Ekman, V. W., 1905: On the influence of the Earth's rotation on ocean-currents. *Ark. Mat. Astron. Fys.,* **2,** 1–53.

Emery, W. J., and R. E. Thomson, 1998: *Data Analysis Methods in Physical Oceanography*. Elsevier, 634 pp.

Essen, H.-H., 1993: Ekman portion of surface currents, as measured by radar in different areas. *Dtsch. Hydrogr. Z.,* **45,** 57–85.

——, K.-W. Gurgel, and F. Schirmer, 1983: Tidal and wind-driven parts of surface currents, as measured by radar. *Dtsch. Hydrogr. Z.,* **36,** 81–96.

Ewing, G. C., 1950: Relation between band slicks at the surface and internal waves in the sea. *Science,* **111,** 91–94.

Fernandez, D. M., J. F. Vesecky, and C. C. Teague, 1996: Measurements of upper ocean surface current shear with high-frequency radar. *J. Geophys. Res.,* **101** (C12), 28 615–28 625.

Golub, G. H., and C. F. van Loan, 1980: An analysis of the total least squares problem. *SIAM J. Numer. Anal.,* **17,** 883–893, doi:10.1137/0717073.

——, M. Heath, and G. Wahba, 1979: Generalized cross-validation as a method for choosing a good ridge parameter. *Technometrics,* **21,** 215–223.

Gonella, J., 1971: The drift current from observations made on the Bouee Laboratoire. *Cah. Oceanogr.,* **23,** 1–15.

——, 1972: A rotary-component method for analysis in meteorological and oceanographic vector time series. *Deep-Sea Res.,* **19,** 833–846.

Ha, E. C., 1979: High-frequency radar measurements of coastal ocean surface currents. Ph.D. thesis, Stanford University, 134 pp.

Hoerl, A. E., and R. W. Kennard, 1970: Ridge regression: Biased estimation for nonorthogonal problems. *Technometrics,* **12,** 55–67.

Huyer, A., and P. M. Kosro, 1987: Mesoscale surveys over the shelf and slope in the upwelling region near Point Arena, California. *J. Geophys. Res.,* **92,** 1655–1681.

Hyder, P., J. H. Simpson, and S. Christopoulos, 2002: Sea-breeze forced diurnal surface currents in the Thermaikos Gulf, North-West Aegean. *Cont. Shelf Res.,* **22,** 585–601.

Kim, S. Y., 2009: Coastal ocean studies in southern San Diego using high-frequency radar derived surface currents. Ph.D. thesis, Scripps Institution of Oceanography, University of California, San Diego, 214 pp. [Available online at http://repositories.cdlib.org/sio/techreport/95/.]

——, E. J. Terrill, and B. D. Cornuelle, 2007: Objectively mapping HF radar-derived surface current data using measured and idealized data covariance matrices. *J. Geophys. Res.,* **112,** C06021, doi:10.1029/2006JC003756.

——, ——, and ——, 2008: Mapping surface currents from HF radar radial velocity measurements using optimal interpolation. *J. Geophys. Res.,* **113,** C10023, doi:10.1029/2007JC004244.

Kirincich, A. R., J. A. Barth, B. A. Grantham, B. A. Menge, and J. Lubchenco, 2005: Wind-driven inner-shelf circulation off central Oregon during summer. *J. Geophys. Res.,* **110,** C10S03, doi:10.1029/2004JC002611.

Kundu, P. K., 1984: Generation of coastal inertial oscillations by time-varying wind. *J. Phys. Oceanogr.,* **14,** 1901–1913.

Large, W. G., and S. Pond, 1981: Open ocean momentum flux measurements in moderate to strong winds. *J. Phys. Oceanogr.,* **11,** 324–336.

LeBlanc, M., and R. Tibshirani, 1996: Combining estimates in regression and classification. *J. Amer. Stat. Assoc.,* **91,** 1641–1650.

Lentz, S. J., 2001: The influence of stratification on the wind-driven cross-shelf circulation over the North Carolina shelf. *J. Phys. Oceanogr.,* **31,** 2749–2760.

Lewis, D. M., and S. E. Belcher, 2004: Time-dependent, coupled, Ekman boundary layer solutions incorporating Stokes drift. *Dyn. Atmos. Oceans,* **37,** 313–351.

Li, Z., and R. H. Weisberg, 1999: West Florida shelf response to upwelling favorable wind forcing: Kinematics. *J. Geophys. Res.,* **104** (C6), 13 507–13 527.

Marquardt, D. W., 1970: Generalized inverses, ridge regression, biased linear estimation, and nonlinear estimation. *Technometrics,* **12,** 591–612.

Munk, W. H., and D. E. Cartwright, 1966: Tidal spectroscopy and prediction. *Philos. Trans. Roy. Soc. London,* **A259,** 533–581.

NOAA, 2006: Harmonic constituents. [Available online at http//www.co-ops.nos.noaa.gov/station_retrieve.shtml?type=Harmonic+Constituents.]

Ng, B., 1993a: The prediction of nearshore wind-induced surface currents from wind velocities measured at nearby land stations. *J. Phys. Oceanogr.,* **23,** 1609–1617.

——, 1993b: Tidal current predictions using rotary empirical orthogonal functions. *J. Atmos. Oceanic Technol.,* **10,** 868–879.

Overland, J. E., and C. H. Pease, 1988: Modeling ice dynamics of coastal seas. *J. Geophys. Res.,* **93** (C12), 15 619–15 637.

Pedlosky, J., 1992: *Geophysical Fluid Dynamics*. 2nd ed. Springer, 710 pp.

Pidgeon, E. J., and C. D. Winant, 2005: Diurnal variability in currents and temperature on the continental shelf between central and southern California. *J. Geophys. Res.,* **110,** C03024, doi:10.1029/2004JC002321.

Prandle, D., 1987: The fine-structure of nearshore tidal and residual circulations revealed by H.F. radar surface current measurements. *J. Phys. Oceanogr.,* **17,** 231–245.

Price, J. F., R. A. Weller, and R. Pinkel, 1986: Diurnal cycling: Observations and models of the upper ocean response to diurnal heating, cooling, and wind mixing. *J. Geophys. Res.,* **91** (C7), 8411–8427.

——, ——, and R. R. Schudlich, 1987: Wind-driven ocean currents and Ekman transport. *Science,* **238,** 1534–1538.

Rabinovich, A. B., G. V. Shevchenko, and R. E. Thomson, 2007: Sea ice and current response to the wind: A vector regressional analysis approach. *J. Atmos. Oceanic Technol.,* **24,** 1086–1101.

Rio, M.-H., and F. Hernandez, 2003: High-frequency response of wind-driven currents measured by drifting buoy and altimetry over the world ocean. *J. Geophys. Res.,* **108,** 3283, doi:10.1029/2002JC001655.

Santiago-Mandujano, F., and E. Firing, 1990: Mixed layer shear generated by wind stress in the central equatorial Pacific. *J. Phys. Oceanogr.,* **20,** 1576–1582.

Schudlich, R. R., and J. F. Price, 1998: Observations of seasonal variation in the Ekman layer. *J. Phys. Oceanogr.,* **28,** 1187–1204.

Simpson, J. H., P. Hyder, T. P. Rippeth, and I. M. Lucas, 2002: Forced oscillations near the critical latitude for diurnal-inertial resonance. *J. Phys. Oceanogr.,* **32,** 177–187.

Smith, D. E., 1959: *A Source Book in Mathematics*. Vol. 1, Dover Publications, 710 pp.

Snee, R. D., 1977: Validation of regression models: Methods and examples. *Technometrics,* **19,** 415–428.

Stewart, R. H., and J. W. Joy, 1974: HF radio measurements of surface currents. *Deep-Sea Res.,* **21,** 1039–1049.

Sverdrup, H. U., 1938: On the process of upwelling. *J. Mar. Res.,* **1,** 155–164.

van Huffel, S., and J. Vandewalle, 1991: *The Total Least Squares Problem: Computational Aspects and Analysis*. SIAM, 314 pp.

Weber, J. E., 1983: Steady wind- and wave-induced currents in the open ocean. *J. Phys. Oceanogr.,* **13,** 524–530.

Weisberg, R. H., Z. Li, and R. Muller-Karger, 2001: West Florida shelf response to local wind forcing: April 1998. *J. Geophys. Res.,* **106** (C12), 31 239–31 262.

Weller, R. A., 1981: Observations of the velocity response to wind forcing in the upper ocean. *J. Geophys. Res.,* **86** (C3), 1969–1977.

——, and A. J. Plueddemann, 1996: Observations of the vertical structure of the oceanic boundary layer. *J. Geophys. Res.,* **101,** 8789–8806.

Winant, C. D., 2004: Three-dimensional wind-driven flow in an elongated, rotating basin. *J. Phys. Oceanogr.,* **34,** 462–476.

Wu, J., 1983: Sea-surface drift currents induced by wind and waves. *J. Phys. Oceanogr.,* **13,** 1441–1451.

Wunsch, C., 1996: *The Ocean Circulation Inverse Problem*. Cambridge University Press, 442 pp.

Zelenke, B. C., 2005: An empirical statistical model relating winds and ocean surface currents: Implications for short-term current forecasts. M.S. thesis, Dept. of Oceanography, Oregon State University, 109 pp. [Available online at http://ir.library.oregonstate.edu/dspace/bitstream/1957/2166/1/Zelenke_Thesis.pdf.]